Article
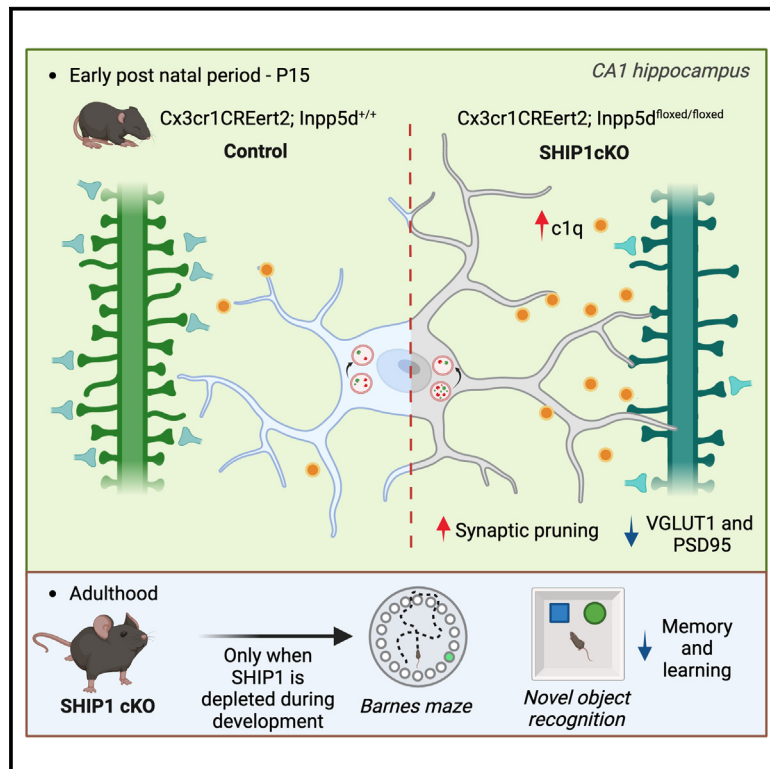
Microglial lipid phosphatase SHIP1 limits complement-mediated synaptic pruning in the healthy developing hippocampus

Graphical abstract

Authors

Alessandro Matera,
Anne-Claire Compagnion,
Chiara Pedicone, ..., Bart J.L. Eggen,
William G. Kerr, Rosa C. Paolicelli

Correspondence

rosachiara.paolicelli@unil.ch

In brief

Inpp5d, which encodes the lipid phosphatase SHIP1, is a risk gene for Alzheimer's disease, but its role in brain development has been poorly studied. Matera, Compagnion et al. demonstrate that Inpp5d is expressed in microglia during early postnatal brain development, where it limits synaptic pruning in a complement-dependent manner, and that its perturbation during brain development has long-lasting effects on cognitive function.

Highlights

- *Inpp5d* is expressed in microglia during early brain development

- SHIP1-deficient microglia show enhanced phagocytic activity and complement expression

- Deleting *Inpp5d* in microglia in the developing brain increases synaptic pruning

- Developmental, but not adult, *Inpp5d* deletion affects adult cognitive function

CellPress

Immunity

Article

Microglial lipid phosphatase SHIP1 limits complement-mediated synaptic pruning in the healthy developing hippocampus

Alessandro Matera,[1,17] Anne-Claire Compagnion,[1,17] Chiara Pedicone,[2,3,18] M. Kotah Janssen,[4,18] Andranik Ivanov,[5] Katia Monsorno,[1] Gwenaël Labouèbe,[1] Loredana Leggio,[6] Marta Pereira,[7,8] Dieter Beule,[5] Virginie Mansuy-Aubert,[1] Tim L. Williams,[9] Nunzio Iraci,[6] Amanda Sierra,[7,10,11] Samuele G. Marro,[12,13,14] Alison M. Goate,[2,3,13] Bart J.L. Eggen,[4] William G. Kerr,[12,15,16] and Rosa C. Paolicelli[1,19,*]

[1]Department of Biomedical Sciences, University of Lausanne, Lausanne, Switzerland
[2]Department of Genetics and Genomics Sciences, Icahn School of Medicine at Mt. Sinai, New York, NY, USA
[3]Ronald M. Loeb Center for Alzheimer's Disease, Icahn School of Medicine at Mount Sinai, New York, NY, USA
[4]Department of Biomedical Sciences, Section Molecular Neurobiology, University of Groningen, University Medical Center Groningen, Groningen, the Netherlands
[5]Core Unit Bioinformatics, Berlin Institute of Health, Charité—Universitätsmedizin, Berlin, Germany
[6]Department of Biomedical and Biotechnological Sciences, University of Catania, 95123 Catania, Italy
[7]Achucarro Basque Center for Neuroscience, Barrio Sarriena s/n, Leioa, Spain
[8]Department of Neuroscience, University of the Basque Country EHU/UPV, Barrio Sarriena s/n, Leioa, Spain
[9]Department of Veterinary Medicine, University of Cambridge, Cambridge, UK
[10]Department of Biochemistry and Molecular Biology, University of the Basque Country EHU/UPV, Barrio Sarriena, Leioa, Spain
[11]Ikerbasque Foundation, Bilbao, Spain
[12]Institute for Regenerative Medicine, Icahn School of Medicine at Mount Sinai, New York, NY, USA
[13]Nash Family Department of Neuroscience, Icahn School of Medicine at Mount Sinai, New York, NY, USA
[14]Department of Neurosciences, Black Family Stem Cell Institute, Icahn School of Medicine at Mt. Sinai, New York, NY, USA
[15]Department of Microbiology & Immunology, SUNY Upstate Medical University, Syracuse, NY, USA
[16]Department of Pediatrics, SUNY Upstate Medical University, Syracuse, NY, USA
[17]These authors contributed equally
[18]These authors contributed equally
[19]Lead contact
*Correspondence: rosachiara.paolicelli@unil.ch
https://doi.org/10.1016/j.immuni.2024.11.003

SUMMARY

The gene inositol polyphosphate-5-phosphatase D (*INPP5D*), which encodes the lipid phosphatase SH2-containing inositol polyphosphate 5-phosphatase 1 (SHIP1), is associated with the risk of Alzheimer's disease (AD). How it influences microglial function and brain physiology is unclear. Here, we showed that SHIP1 was enriched in early stages of healthy brain development. By combining *in vivo* loss-of-function approaches and proteomics, we discovered that mice conditionally lacking microglial SHIP1 displayed increased complement and synapse loss in the early postnatal brain. SHIP1-deficient microglia showed altered transcriptional signatures and abnormal synaptic pruning that was dependent on the complement system. Mice exhibited cognitive defects in adulthood only when microglial SHIP1 was depleted early postnatally but not at later stages. Induced pluripotent stem cell (iPSC)-derived microglia lacking SHIP1 also showed increased engulfment of synaptic structures. These findings suggest that SHIP1 is essential for proper microglia-mediated synapse remodeling in the healthy developing brain. Disrupting this process has lasting behavioral effects and may be linked to vulnerability to neurodegeneration.

INTRODUCTION

Inositol polyphosphate-5-phosphatase D (*INPP5D*) encodes for SH2-containing inositol polyphosphate 5-phosphatase 1 (SHIP1). Recent genome-wide association studies have identified *INPP5D* as both a risk and a protective gene associated with sporadic Alzheimer's disease (AD), supporting a potential role for SHIP1 in providing vulnerability to pathology.[1–4] However, the cellular mechanisms underlying the contribution of SHIP1 dysfunction in neurodegeneration have been so far insufficiently investigated. *INPP5D* is predominantly expressed by microglia in the central nervous system (CNS), both in mice and humans.[5,6] SHIP1 is a multifunctional protein with both enzymatic and scaffold activities.[7,8] On the one hand, it removes
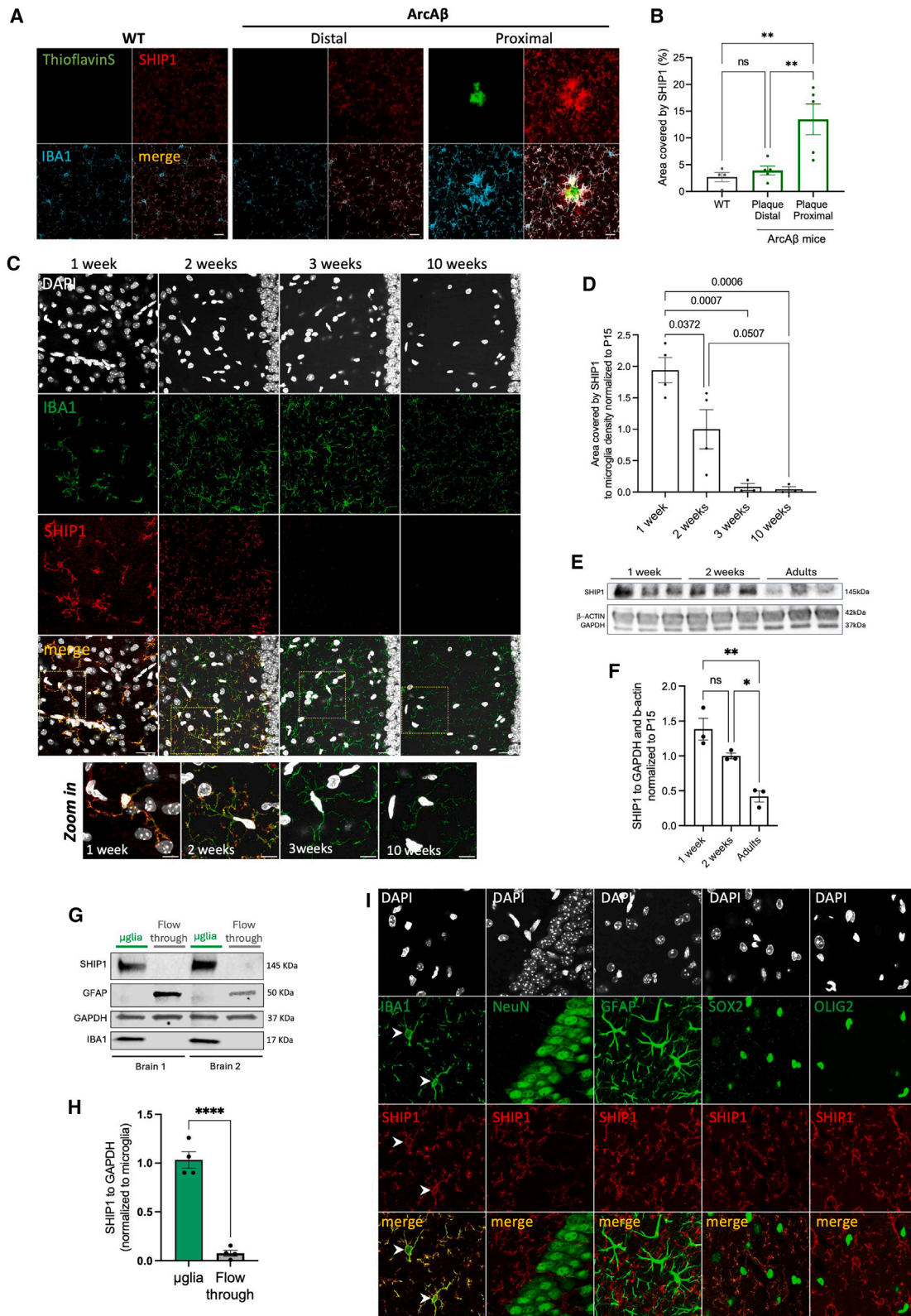
Figure 1. SHIP1 is expressed in the early postnatal brain

(A) Confocal z stack projections of cortex from WT and ArcAβ mice, stained for SHIP1, IBA1, and thioflavin-S. Plaque-distal microglia were imaged at least 400 μm far from Aβ plaques. Scale bar, 10 μm.

(legend continued on next page)

Immunity
Article

CellPress
OPEN ACCESS

the 5′ phosphate from the inositol phospholipid PI(3,4,5)P3, to generate PI(3,4)P2. Of note, phosphoinositides are largely implicated in membrane remodeling and trafficking required for efficient phagocytosis.[9,10] On the other hand, SHIP1 can be recruited to tyrosine-phosphorylated receptor tails through its SH2 domain at the plasma membrane. Once there, it binds to phosphorylated immunoreceptor tyrosine-based activation (ITAM) and inhibition (ITIM) motifs of adaptor proteins such as DNAX activating protein of 12 kDa (DAP12) and FcRγ. This binding blocks the site for SYK tyrosine-protein kinase, thus inhibiting downstream signaling from surface receptors, including the triggering receptor expressed on myeloid cells 2 (TREM2) and the complement receptor 3 (C3R).[8,11] Therefore, SHIP1 has multiple functions and may influence microglial intracellular signaling through both phosphatase-dependent and independent mechanisms.

Growing evidence indicates that, in sporadic neurodegenerative disorders, synaptic alterations and microglial dysfunction occur at early preclinical stages, long before the first symptoms appear.[12] Microglia, in particular, are emerging as key players in the pathogenesis of brain disorders, with a prominent fraction of epigenomic signals and single nucleotide polymorphisms (SNPs) associated with neurodegeneration found to be highly enriched in this cell type.[13–15] Microglia not only rapidly react to any brain insult but are also extensively involved in physiological processes, such as synapse remodeling and circuit refinement, particularly during brain development. At early postnatal stages, microglia display high cellular heterogeneity and transcriptomic signatures that, to some extent, resemble microglial states associated with diseases,[16–19] drawing a fascinating parallelism between immature and disease-associated microglia (DAM).

Here, we found that microglial SHIP1 is not only a hallmark of plaque-associated microglia in a mouse model of AD, but it is also expressed in the developing brain of wild-type mice (WT), where it modulates physiological functions. Using a microglial and macrophage SHIP1 conditional knockout (cKO) mouse model, in combination with transcriptomics, proteomics, and imaging approaches, we showed that SHIP1 limits complement-mediated synapse remodeling for proper brain development. Inducing microglial dysfunction via SHIP1 depletion during brain development was enough to reproduce features of cognitive decline in adult mice with deficits or delays in episodic and spatial memory. Depleting SHIP1 after development did not lead to cognitive defects in adulthood, consistent with a role for microglial SHIP1 specifically at early postnatal stages. Human induced pluripotent stem cell (iPSC)-derived microglia (iMG) lacking SHIP1, in line with mouse data, also showed an increased engulfment of synaptic structures.

Overall, these findings indicate that SHIP1 plays a crucial role in controlling important microglial functions during early brain development and in regulating microglia-mediated synaptic pruning via the complement system. Therefore, microglial SHIP1, previously linked primarily to AD, may contribute to the cascade of underlying molecular and cellular events in early pre-symptomatic stages.

RESULTS

Microglial SHIP1 is expressed at early developmental stages

SHIP1 protein amount has been reported to increase both in the brain of AD patients and in mouse models of AD, as compared with healthy controls or WT littermates.[20,21] Using ArcAβ mice, which overexpress the human amyloid precursor protein carrying the Arctic and Swedish mutations,[22] we quantified SHIP1 immunoreactivity in microglia located proximally or distally to amyloid beta (Aβ) plaques and compared it to microglia from age-matched WT mice (Figures 1A and 1B). While the protein amount was significantly higher in plaque-associated microglia than in distal cells from AD mice, there were no differences between the latter and cells from WT mice (Figures 1A and 1B), suggesting that microglial SHIP1 is specifically upregulated in response to amyloid deposits and not as a mere consequence of a broad pathological condition.

Collective evidence suggests that microglial states associated with brain diseases can partially resemble those found in brain development, when these cells are particularly engaged in a variety of biological processes, including scavenging of apoptotic neurons and refinement of neuronal circuits.[16–18,23] Consistently, several microglial genes upregulated in pathology are also highly expressed in the developing brain, e.g., complement molecules and TREM2.[16–18,23] Thus, we first asked whether also SHIP1 was subjected to dynamic regulation across the lifespan. SHIP1 protein was detected in the two first postnatal weeks while being decreased in young adult hippocampus (Figures 1C, 1D, and S1A). The increased expression of SHIP1 in the early postnatal brain was further confirmed by western blot (WB) and ELISA immunoassay (Figures 1E, 1F, and S1B). These findings are in apparent contradiction with previously published dataset that reports high expression of *Inpp5d* mRNA in microglia from adult mouse brains.[5,16,24] To investigate this aspect, we assessed *Inpp5d* mRNA by RT-qPCR in hippocampal and cortical samples, isolated from WT mice at postnatal days (P)15 and P70, and we measured in parallel SHIP1 protein by immunofluorescence. In the hippocampus, both mRNA and protein were reduced in adults as compared with P15 (Figures 1C, 1D, and

---

(B) Relative quantification of (A), showing the area covered by SHIP1 (%). One-way ANOVA, Tukey's multiple comparison test: **$p < 0.01$. $N = 4$ WT, $N = 5$ ArcAβ mice.

(C) Confocal z stack projections showing DAPI, IBA1, and SHIP1 in CA1 hippocampus of WT mice at 1 week ($N = 4$), 2 weeks ($N = 4$), 3 weeks ($N = 3$), and 10 weeks ($N = 3$) of age. Scale bar, 30 μm; zoom-in: 10 μm.

(D) Relative quantification of (C), normalized to P15 time point. One-way ANOVA, Tukey's multiple comparison test.

(E and F) (E) Representative WB of SHIP1, β-actin, and GAPDH and (F) relative quantification of hippocampal homogenates from WT mice 1 week ($N = 3$), 2 weeks ($N = 3$), and 12–14 weeks old ($N = 3$). One-way ANOVA, Tukey's multiple comparison test. *$p < 0.05$, **$p < 0.01$. Average of two independent technical replicates.

(G and H) (G) Representative WB of SHIP1, GFAP, IBA1, and GAPDH and (H) relative SHIP1 quantification of magnetic-activated cell sorting-isolated microglia from the whole P15 brain, compared with the respective flowthrough. $N = 4$ WT mice. Unpaired t test, ****$p < 0.0001$.

(I) Confocal z stack projections of hippocampi from WT mice, co-stained for SHIP1 and IBA1, NeuN, GFAP, SOX2, or OLIG2. White arrows highlight SHIP1-IBA1 colocalization. Scale bar, 20 μm. Multiple ROIs have been analyzed per animal over independent technical experiments. Statistics are performed per animal.
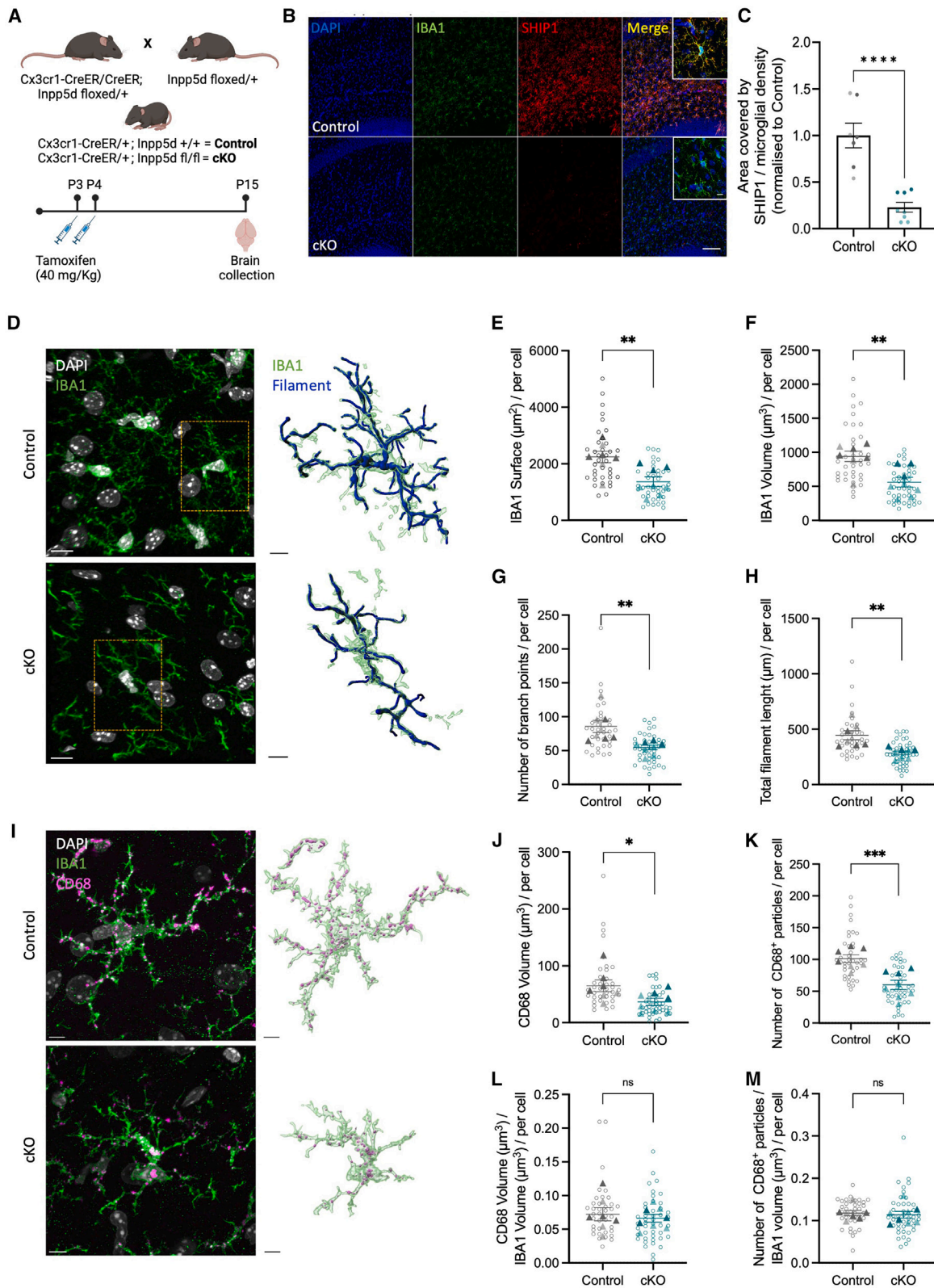
Figure 2. SHIP1 KO microglia show reduced morphological complexity

(A) Experimental breeding and timeline.

(B) Confocal z stack projections of the CA1 hippocampus stained for DAPI, IBA1, and SHIP1, in control and cKO P15 mice. Scale bar: 100 μm; zoom-in: 10 μm.

S1C), consistent with our earlier findings. However, in cortical samples, *Inpp5d* mRNA was similarly high at P15 and in adults (Figure S1C), in line with published data reporting high levels of *Inpp5d* transcripts in the adult brain.[5,16,24] Yet, SHIP1 immunoreactivity was clearly reduced in the cortex of adult mice compared with P15 (Figure S1D). Next, to investigate the cellular source of SHIP1 in the early postnatal brain, we isolated microglia from the brains of WT mice at P15 using magnetic cell sorting. SHIP1 was only detectable in the microglia-enriched samples, while it was not expressed in the flowthrough, which contains all other brain cells (Figures 1G and 1H). Additionally, we co-stained brain slices from WT mice at P15 for SHIP1 and different cell identity markers, confirming that SHIP1 only co-localizes with the microglial marker IBA1 and not with neuronal (NeuN), astrocyte (GFAP), oligodendrocyte (OLIG2), or neural stem cell (SOX2) markers (Figure 1I).

Taken together, these findings support a dynamic regulation of microglial SHIP1 not only in the context of established AD pathology but also in the healthy developing brain.

Loss of microglial SHIP1 results in reduced microglial complexity

To better understand the functional role of microglial SHIP1 in the developing brain, we generated an inducible cKO mouse line by crossing *Cx3cr1*-CreERT2 and *Inpp5d*-floxed strains.[25,26] Our breeding strategy was designed to obtain all the experimental subjects as littermates, heterozygous for Cre expression and carrying or not the *Inpp5d* gene flanked by *loxP* sites, thus generating $Cx3cr1^{CreERT2/+};Inpp5d^{fl/fl}$ and $Cx3cr1^{CreERT2/+};Inpp5d^{+/+}$ mice (Figure 2A). For simplicity, we will refer to these mice as cKO and control, respectively. Cre-mediated deletion of *Inpp5d* was achieved by two consecutive tamoxifen (TAM) injections at P3 and P4, leading to a reduction of both mRNA (Figure S2A) and protein (Figures 2B, 2C, S2B, and S2C) at P15. We further confirmed that SHIP1 immunoreactivity was detectable in the hippocampus of P15 control mice but not in adults, while the signal was absent in cKO mice at both ages (Figure S2D). Microglial density in this region was not affected in cKO mice, while the total area covered by IBA1 immunoreactivity showed a trend for decrease (Figures S2E–S2G). Three-dimensional (3D) reconstruction of confocal acquisitions and subsequent morphometric analysis revealed a decrease in the surface and volume of IBA1+ cells (Figures 2D–2F). Filament analysis also showed a reduction in the total filament length and the branch points per cell (Figures 2D, 2G, and 2H) in SHIP1 KO microglia, indicative of reduced complexity, while the average length was not affected (Figure S2H). Next, we asked whether the loss of SHIP1 could alter the content of phagocytic structures within microglia. We

quantified the number and volume of CD68+ phagolysosomes per cell and found that both were reduced at P15 (Figures 2I–2K). However, these parameters were not different when normalized to the cell volume (Figures 2L and 2M), indicating that, in proportion to their size, SHIP1 WT and KO microglia have comparable phagolysosomal structures. It is noteworthy that microglial volume and complexity were also reduced in the cortex and cerebellum of P15 cKO mice, indicating that these morphological changes are broadly present across the brain (Figures S2I–S2M). Overall, these data show that the loss of SHIP1 in microglia leads to a reduction in morphological complexity, which may reflect potential alterations in microglial surveillance and phagocytic activity.

SHIP1 KO microglia exhibit altered transcriptional signature and increased phagocytosis

To deepen into potential alterations in microglial function, we examined the transcriptional signature of SHIP1 KO microglia by bulk RNA sequencing on cells sorted from the hippocampi of P15 control and cKO littermates (Figure 3A). Transcriptomic analysis identified 545 differentially expressed genes (DEGs), of which 194 were upregulated and 351 downregulated in KO microglia (adj *p* value < 0.1, Figure 3B; Table S1). Gene set enrichment analysis (GSEA)[27] revealed that cell migration, regulation of natural killer (NK) cells chemotaxis, and regulation of tau protein kinase activity were increased, among others (Figures 3C and S3A), while cell cycle, cell division, and interferon response genes were downregulated in KO cells (Figures S3A–S3I). Of note, among the upregulated genes were *Itgax*, *Clec7a*, *Cd63*, *Cd83*, *Csf1*, *Ccl3*, *Ccl4*, *Ccl6*, *Ccl9*, *Egr1*, *Famc20*, *Serpin2*, and *Ank* (Figure 3B), which are commonly enriched in microglial signatures associated with development and disease.[16–18,28,29,30] Further analyses highlighted that about 18% and 17% of the DAM and axonal trait-associated microglial signatures (ATM),[16] respectively, were represented among the DEGs in SHIP1 KO microglia (Table S1).

Since SHIP1 acts as a negative regulator of TREM2 activity,[8] we hypothesized that at least some transcriptional alterations in SHIP1 KO microglia might be driven by enhanced TREM2 signaling. Indeed, the DAM program has been shown to progress from an initial stage (DAM1) to a subsequent stage (DAM2) depending on TREM2.[28,29] Consistent with this, we found that some of these DAM2 genes were also substantially dysregulated in our dataset (Figures 3D and 3E). To validate our bulk RNA-seq data, we performed immunostaining for one of the DEGs, the C-type lectin domain family 7 member A (*Clec7a*), in the CA1 region of the hippocampus of cKO and control littermates. CLEC7A protein has been recently identified as an ATM-like marker in the fetal brain,[32] and it was previously

---

(C) Quantification of the area covered by SHIP1 normalized to the microglial number. *N* = 7 control vs. *N* = 8 SHIP1 cKO mice. Unpaired t test, ****$p < 0.0001$.

(D–H) (D) Confocal z stack projections and 3D reconstruction of IBA1 surface and microglial filaments. Reconstructed cells are highlighted in yellow. Scale bar acquisition: 10 μm; scale bar 3D reconstruction: 5 μm. Quantification of microglial morphology, showing (E) IBA1 surface, (F) IBA1 volume, (G) number of branch points, and (H) total filament length. Control: *n* = 36–38 cells vs. cKO *n* = 42–46 cells reconstructed from *N* = 7 control vs. *N* = 8 SHIP1 cKO mice. Unpaired t test, **$p < 0.01$.

(I) Confocal z stack projections and 3D reconstruction of IBA1 and CD68$^+$ structures. Scale bar: 5 μm.

(J–M) Quantification of (I), indicating CD68 (J) volume and (K) number per microglia, also normalized to respective IBA1 volume (L and M). Control *n* = 38 cells vs. cKO *n* = 44 cells, reconstructed from *N* = 7 control vs. *N* = 8 SHIP1 cKO mice. Unpaired t test, *$p < 0.05$, ***$p < 0.001$. Animals are represented with triangles, whereas cells with circles. Females are indicated in light and males in dark colors. Multiple ROIs have been analyzed per animal. Statistics are performed per animal.
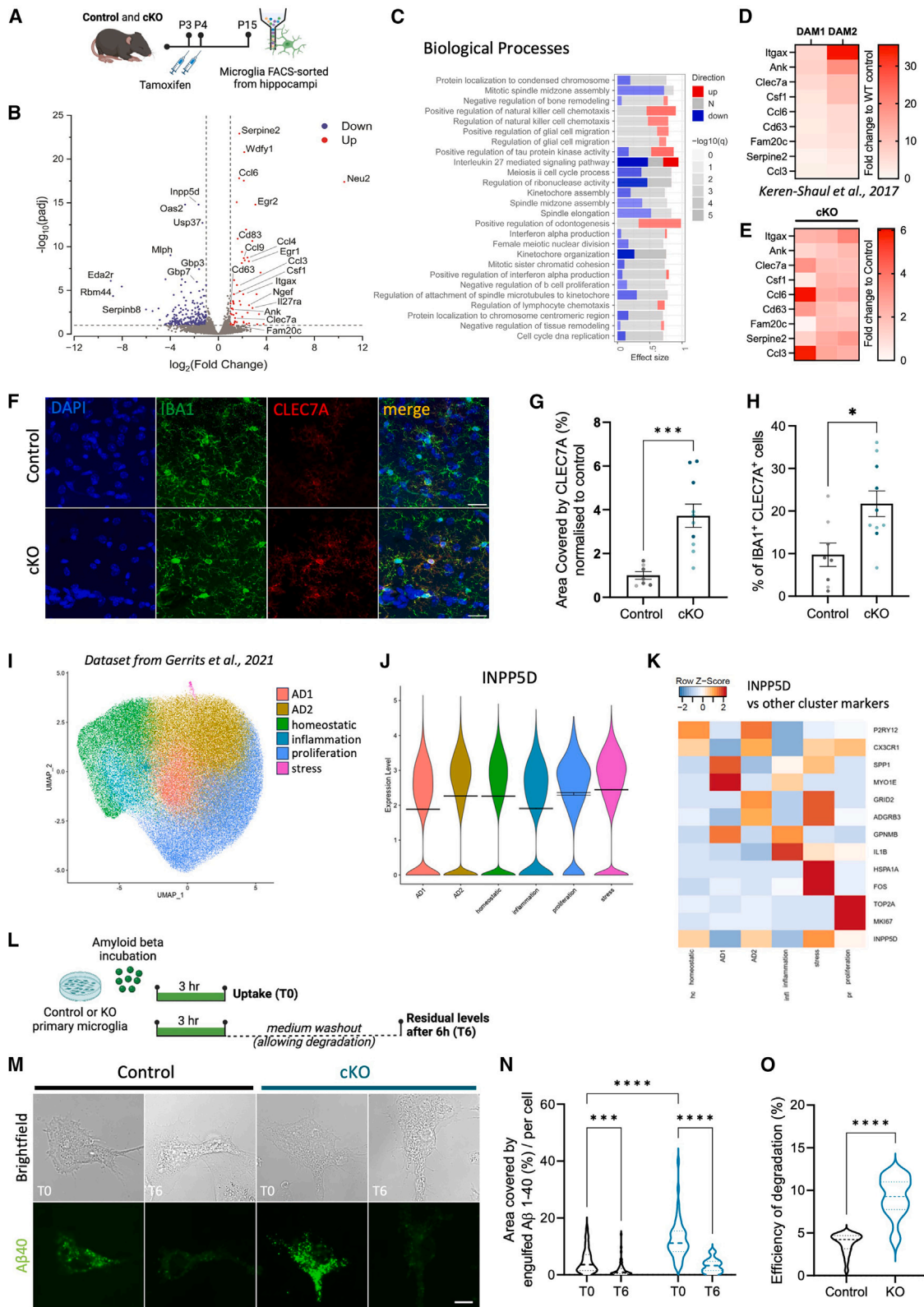
(legend on next page)

shown to be increased in plaque-associated microglia lacking SHIP1, in a mouse model of AD.[33] Consistently, we observed a significant increase in the area covered by CLEC7A and in the fraction of CLEC7A+ microglia in the hippocampus of cKO mice at P15 (Figures 3F–3H). Another gene significantly upregulated in SHIP1 KO microglia was *Cd63*, a member of the transmembrane tetraspanin family. The CD63 protein is highly enriched at the membrane of extracellular vesicles (EVs),[34] and it has been proposed to regulate EV biogenesis.[35] Thus, we asked whether microglia lacking SHIP1 would release more EVs. To this aim, we isolated EVs from the conditioned medium of CRISPR-Cas9 SHIP1 KO clones and parental BV2 cell lines that we had previously generated[36] (Figure S3J). Nanoparticle tracking analysis revealed that, while the modal size of EVs was comparable between genotypes (100–200 nm), the total number of particles was significantly increased in the medium collected from KO cells (Figures S3K–S3M).

Overall, the upregulation of several DAM genes suggests that the loss of SHIP1 favors the emergence of the DAM signature, consistent with previous data in mouse model of AD.[33,37] Thus, we asked whether a similar pattern could be seen in the brains of AD donors. We interrogated the database from Gerrits et al.,[31] in which snRNA-seq was performed on control and AD brains containing only Aβ plaques or both Aβ and tau pathology. In this study, distinct expression profiles of microglia were described, and in particular, a signature of phagocytic microglia associated with Aβ, named AD1. In line with our findings, the expression of *INPP5D* mRNAs in this cluster was lower compared with those in homeostatic microglia (Figures 3I–3K), suggesting an inverse correlation between *INPP5D* expression and the microglial response to Aβ. This prompted us to investigate the phagocytic capacity of microglia lacking SHIP1. Primary microglia from control and cKO mice were fed with fluorescently labeled Aβ40 peptide and, after 3 h incubation, the engulfed cargo was chased for degradation for additional 6 h (Figures 3L–3O). SHIP1 KO cells not only engulfed more Aβ than controls but were also more efficient in degradation (Figures 3M–3O). Overall, loss of SHIP1 in microglia induces transcriptional alterations partially overlapping with microglial states found at times of high phagocytic activity, both in the developing brain and in disease conditions, and it enhances phagocytic capacity toward Aβ.

Depletion of microglial SHIP1 leads to the upregulation of the complement system and synapse loss

To investigate in an unbiased fashion the potential effects of SHIP1 KO microglia in the entire developing hippocampus, we employed an untargeted proteomics-based approach, comparing hippocampi dissected from control and cKO littermates at P15 (Figure 4A). Our analysis identified 7477 different protein IDs (Table S1). CERNO GSEA[27] detected only 3 significant gene sets differentially regulated in SHIP1 cKO compared with controls: complement activation, synapse pruning, and humoral immune response (Figure 4B). Among the top peptides, we observed an enrichment of the subunits C1qa, C1qb, and C1qc, which form the complement component 1q (C1q). These findings were confirmed by immunoreactivity in brain slices, showing higher C1q protein in cKO mice both within microglial cells (Figures 4C and 4D) and in the extracellular compartment (Figures 4E and 4F) compared with control littermates. Of note, C1q complement in the plasma was not different at P15 (Figure S4A).

The complement system is one of the most well-characterized "eat me" signals for synapse elimination, both in development and at early stages of AD.[38–40] Therefore, we hypothesized that an increased deposition of complement may lead to excessive synapse loss. To test this possibility, we stained P15 hippocampal slices against the pre- and postsynaptic markers VGLUT1 and PSD95. Confocal imaging and relative quantification of synaptic puncta showed a significant decrease in both markers in the CA1 *stratum radiatum* of cKO mice (Figures 4G–4I). VGLUT1-PSD95 apposition, as a proxy of synapses, was also decreased (Figures 4J and 4K). These findings indicate that the number of synapses in the hippocampal CA1 region of cKO mice is remarkably reduced. While the reduction in PSD95 was also confirmed by WB performed on hippocampal homogenates (Figures S4B and S4C), this was not the case for VGLUT1 (Figures S4B and S4D), suggesting some potential region-specific effect. To investigate this aspect, we quantified VGLUT1 immunoreactivity in the hippocampal CA1 and CA3 regions, confirming a decrease only in the CA1 area (Figures S4G–S4J). By contrast, the decrease in PSD95 was confirmed in both the hippocampal CA1 and CA3 structures (Figures S4K–S4N). WB analysis also revealed a reduction in the inhibitory marker VGAT, while Gephyrin remained unchanged (Figures S4B, S4E,

---

Figure 3. SHIP1 KO microglia display altered transcriptional profile and enhanced phagocytosis

(A) Experimental pipeline for bulk-RNA-seq experiment.

(B) Volcano plot of DEGs identified by RNA-seq analysis ($N = 4$ control vs. $N = 3$ SHIP1 cKO male mice). Genes highlighted are significantly modulated with a log_2fold change > 1.3 (cutoff: p-adj < 0.1).

(C) Msig-DB gene ontology biological processes significantly enriched in SHIP1 KO microglia.

(D and E) (D) Expression changes of Trem2-dependent DAM2 genes identified in AD mice in Keren-Shaul et al.,[28] and (E) in our dataset (each column is the logFC of each replicate over the average of control samples).

(F) Confocal z stack projections of the CA1 hippocampus, showing the increase of CLEC7A protein in SHIP1 cKO mice. Scale bar: 20 μm.

(G and H) (G) Relative quantification of CLEC7A area covered normalized to control and (H) percentage of double-positive IBA1 and CLEC7A cells. Unpaired t test, $*p < 0.05$, $***p < 0.001$. $N = 7$ control vs. $N = 10$ SHIP1 cKO mice. Females are indicated in light, and males are in dark colors. Statistics are performed per animal.

(I and J) (I) UMAP of different human microglia and (J) expression of *INPP5D* in the different microglial clusters identified in Gerrits et al.[31]

(K) Expression of *INPP5D* compared with other markers for the different microglial clusters identified.

(L) Experimental scheme for Aβ engulfment and degradation assay.

(M) Confocal z stack projections of primary SHIP1 KO and control microglia, exposed to fluorescently labeled-488 Aβ for cargo uptake (T0) and degradation (T6).

(N and O) (N) Relative quantification of area covered by Aβ per cell, and (O) efficiency of degradation. Scale bar: 10 μm. In (N), two-way ANOVA, Tukey's multiple comparison test: $***p < 0.001$, $****p < 0.0001$. In (O), unpaired t test, $****p < 0.0001$. T0: control $n = 77$ cells, KO $n = 49$ cells. T6: control $n = 58$ cells, KO $n = 40$ cells. Data are averaged from $N = 3$ control and $N = 3$ KO-independent primary microglia preparations.

Immunity
Article

(legend on next page)

Immunity
Article

CellPress
OPEN ACCESS
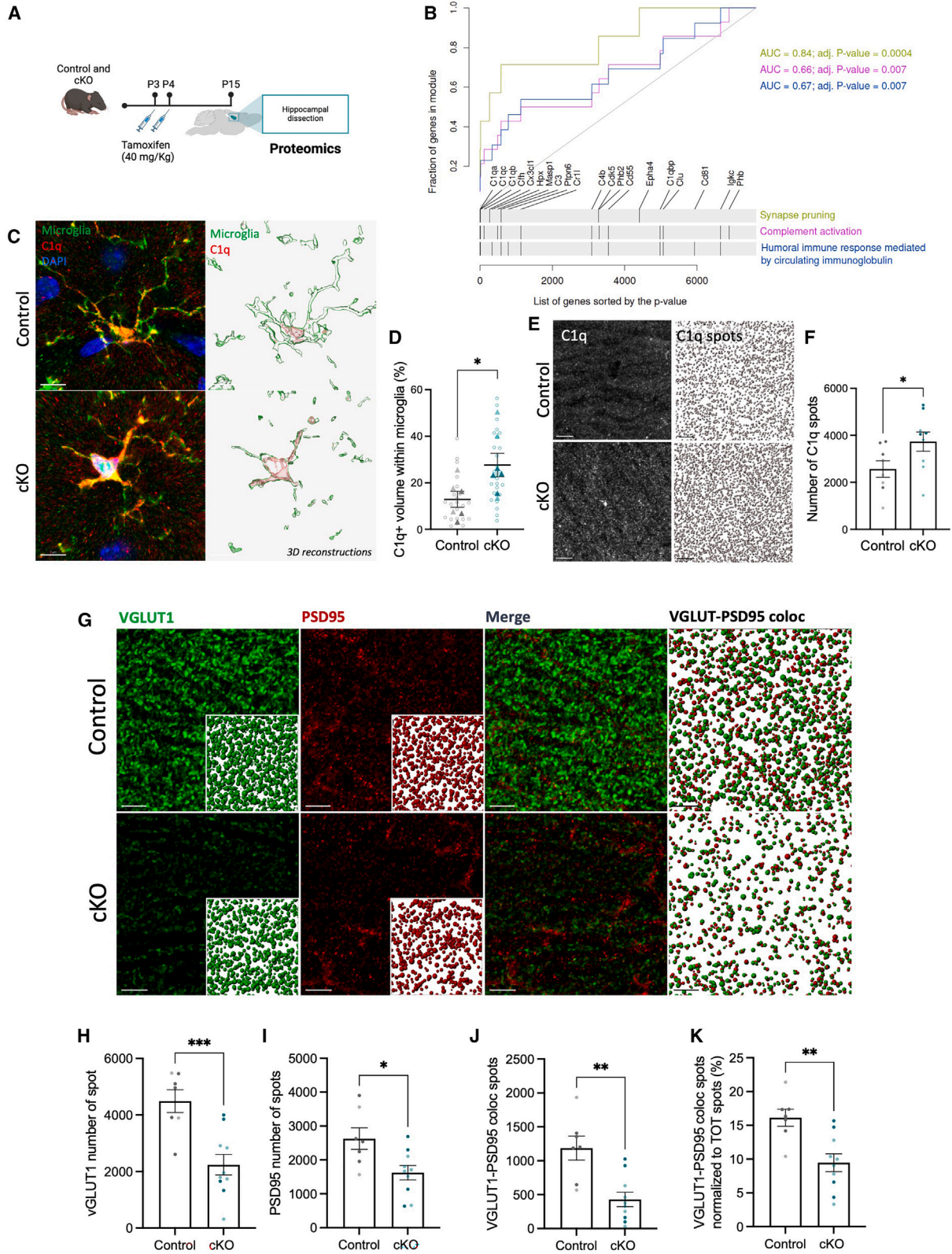
and S4F). A decrease in VGLUT1 and PSD95 by immunostaining was also observed in the cortex of cKO mice (Figures S4O–S4R). However, whole-cell recordings of CA1 pyramidal neurons in brain slices from P15 mice did not reveal any significant change in the spontaneous and miniature excitatory postsynaptic currents (sEPCSs and mEPCSs, respectively; Figures S4S–S4X), suggesting compensatory mechanisms despite the synapse loss in cKO mice.

snRNA-seq analysis predicts decreased synaptic communication in the hippocampal neurons of cKO mice

To further investigate potential consequences on hippocampal neurons, we performed single-nucleus RNA sequencing (snRNA-seq) on the whole hippocampus of control and cKO mice at P15 (Figure 5A). We detected all major cell types in the mouse hippocampus (Figures 5B and 5C; Table S2), including subtypes of excitatory and inhibitory neurons (Figures S5A–S5E, Table S2). Several genes were differentially expressed between control and cKO mice across the identified cell types (Table S2; Figures S5F and S5G), particularly in excitatory hippocampal neurons (Figure 5D). Gene Ontology analysis of the DEGs enriched in excitatory hippocampal neurons from cKO mice using a synapse-specific database[41] revealed an enrichment of postsynaptic structural organization and presynaptic vesicle cycling terms (Figure 5E; Table S2), which might reflect the compensation observed in our electrophysiological data (Figures S4S–S4X). We then assessed predicted differences in cell-cell communication between control and cKO mice using CellChat.[42] This analysis revealed a reduction in the strength of cell-cell interactions in the cKO hippocampus (Figure 5F), accompanied by an increase in the total number of interactions (Figure 5G), especially within excitatory and inhibitory neuronal subtypes. This change to neuronal interactions might be in part mediated by microglia, which were predicted in cKO mice to contribute less to the neuregulin signaling pathway, involved in neuronal survival and synaptogenesis[43] (Figure 5H). In line with our findings of increased inflammatory and disease-associated signatures in cKO mice, microglia from this group were also predicted to have decreased signaling of the immune checkpoint regulator VISTA[44] (Figures 5H and 5I), specifically toward astrocytes, certain neuronal subtypes, and oligodendrocytes (Figure 5J). To identify common pathways altered in neurons, we collapsed the neuronal clusters into excitatory-hippocampal, excitatory-entorhinal, and inhibitory groups and re-ran CellChat

(Figures S5A–S5G). Excitatory neurons from the cKO hippocampus were predicted to send and receive less signaling for a variety of pathways involved in synapse assembly, i.e., neurexins,[45] netrins,[46] ephrins,[47] cell adhesion molecules,[48] and dystroglycans[49] (Figure 5J), in line with the synaptic loss we described. These signaling changes were predicted to be decreased primarily between excitatory hippocampal neurons and all other neuronal groups but also in their communication with other CNS cell types (i.e., astrocytes, oligodendrocytes, OPCs, Figure S5J). The loss of synapse-related pathways was also observed in interneurons from cKO mice (Figure S5K), in line with the decrease in VGAT (Figures S4B and S4F). Overall, these data point to a global disruption in cell-cell communication involving neurons in the hippocampus of cKO mice.

Microglia lacking SHIP1 show abnormal synaptic pruning

Microglia are key cellular mediators of synaptic pruning in early brain development and in pathological contexts.[38–40,50–53] Given the increased phagocytic phenotype induced by SHIP1 depletion as shown in Figures 3M–3O, and in light of the prominent C1q increase in cKO mice (Figures 4C–4F), we hypothesized that microglia might be directly implicated in the observed synapse loss through enhanced pruning. To test this hypothesis, we performed live imaging on primary microglia exposed to synaptosomes. WT and SHIP1 KO cells were fed for 1 h with synaptosomes conjugated with the pH-sensitive dye pHrodo. After washout, the intracellular signal was quantified as a proxy of uptake (T0) and followed over time. The residual signal after 6 h (T6) was considered to reflect cargo degradation (Figure 6A). Time-lapse quantification showed that, after medium washout, the load of the internalized cargo progressively decreased over time. In control microglia, the intracellular signal significantly differed from the initial amount (T0) starting at 5 h, indicating that 6 h is a suitable time point to assess degradation (Figures S6A and S6B). In SHIP1 KO microglia, this difference was already detectable 2 h after medium washout (Figures S6A and S6B), in line with a more efficient degradation quantified at 6 h (Figures 6B–6D; Videos S1 and S2). pHrodo detection within microglia was absent following incubation with bafilomycin or cytochalasin D, inhibitors of lysosomal acidification and phagocytosis, respectively, confirming signal specificity (Figures S6C–S6F). Similar findings were also obtained using tdTomato-labeled synaptosomes (Figures S6G–S6I), confirming that the loss of SHIP1 in microglia promotes both uptake and

---

Figure 4. Complement and synapse loss are enhanced in the developing hippocampus of SHIP1 cKO mice

(A) Pipeline for proteomics on hippocampi from control and cKO P15 mice (N = 3 control; N = 3 cKO per sex).

(B) Evidence plot for the enrichment of all significant biological processes identified in the gene set enrichment analysis. x axis represents the sorted (by p value) gene name (peptide) list. y axis is the cumulative fraction of the genes (peptides) in a given gene set. Cutoff: adj p value < 0.05.

(C and D) (C) Confocal z stack projections and relative 3D reconstruction of C1q immunoreactivity within microglia in the hippocampal CA1 of control and SHIP1 cKO mice at P15; scale bar: 7 μm, and (D) relative quantification showing the percentage of C1q+ volume within microglia. Cells: n = 22 control and n = 26 cKO from N = 6 control and N = 7 cKO mice. Unpaired t test, *p < 0.05.

(E and F) (E) Confocal z stack projections and relative spots 3D reconstruction of C1q staining in CA1 hippocampus of control and SHIP1 cKO mice at P15 (scale bar: 5 μm), and (F) relative quantification showing the number of C1q spots. N = 8 control vs. N = 9 SHIP1 cKO mice. Unpaired t test, *p < 0.05.

(G–I) (G) Confocal z stack projections of CA1 hippocampus stained for DAPI, vGLUT1, and PSD95, along with their relative spot 3D reconstruction at P15. Relative quantification of (H) VGLUT1 and (I) PSD95 number of spots.

(J and K) (J) Quantification of colocalized VGLUT1 and PSD95 structures and (K) ratio of the colocalized spots to their total number. Scale bar: 5 μm. N = 7 control vs. N = 10 cKO mice. Unpaired t test, *p < 0.05, **p < 0.01, ***p < 0.001. Multiple ROIs and sections have been analyzed per animal. Statistics are performed per animal. Females are indicated in light and males in dark colors in all the graphs.

CellPress
OPEN ACCESS

Immunity
Article
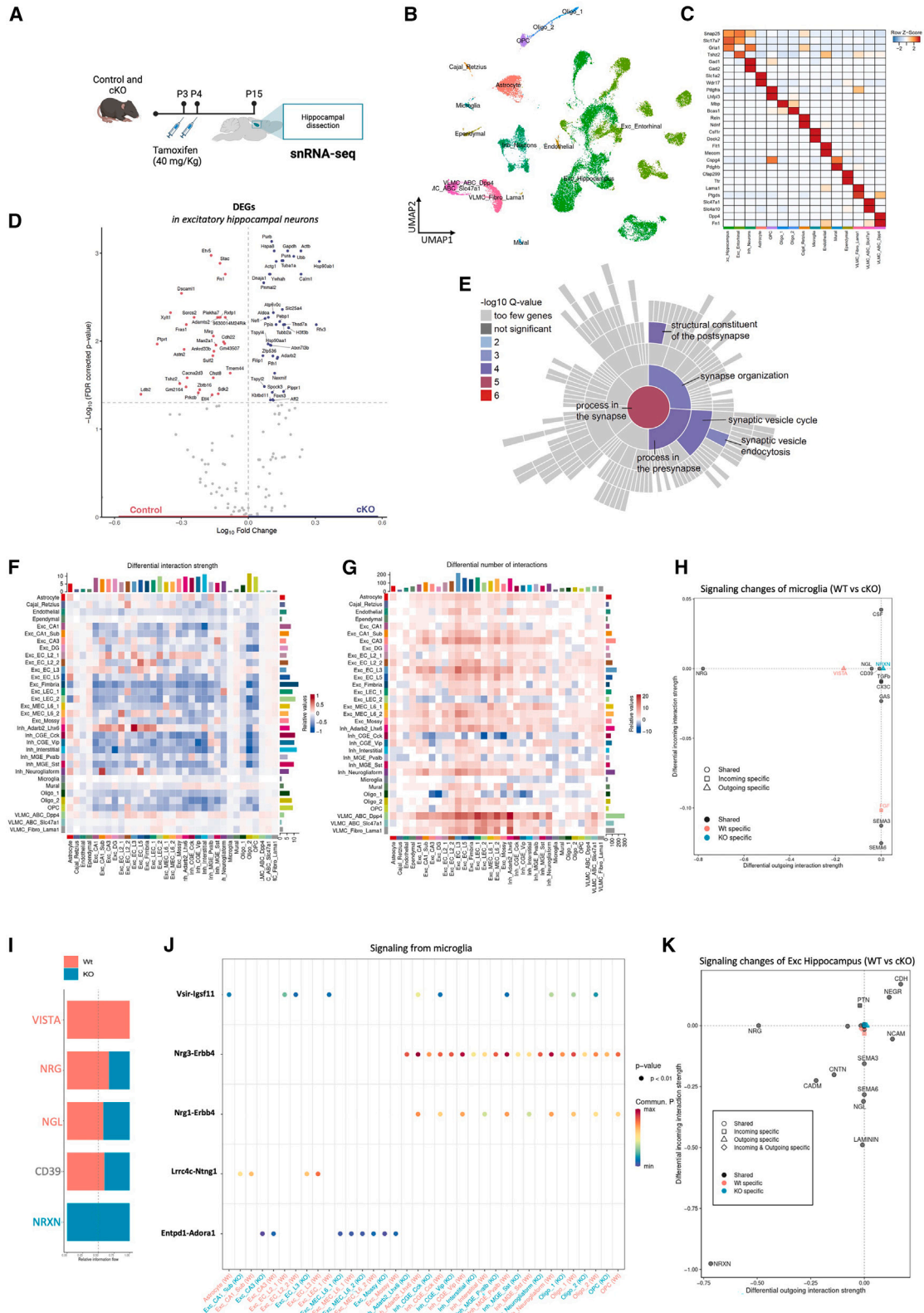
Figure 5. snRNA sequencing analysis predicts weakened neuron-neuron interactions in the SHIP1 cKO hippocampus
(A) Experimental design of snRNA-seq on hippocampi from control and cKO P15 (N = 4 control and N = 4 cKO, both sexes).
(B) Unbiased clustering of snRNA-seq data from 47,313 nuclei, represented on a UMAP, identifying 15 different clusters.

(legend continued on next page)

degradation of synaptic structures, thus enhancing the phagocytic efficiency. The degradation of synaptosomes is lysosomal-dependent, as it is completely prevented by treatment with bafilomycin (Figures S6L–S6O). Furthermore, after treatment with bafilomycin, the intracellular load of synaptosomes was significantly higher in SHIP1 KO cells compared with controls, consistent with an increased uptake (Figures S6M and S6N).

To further confirm these findings, we quantified synapse engulfment *in vivo* at two different time points, P12 and P15, to capture a critical temporal window for microglia-mediated synaptic pruning. Confocal acquisitions of the hippocampal CA1 immunostained for IBA1, CD68, and PSD95 revealed that at P12 the volume and number of PSD95 within microglial phagolysosomes were significantly higher in cKO mice (Figures 6E–6H), indicating increased internalization of synaptic puncta. On the contrary, at P15 the number and volume of PSD95+ puncta within microglial phagolysosomes in cKO were lower than in those from control mice (Figures 6I–6L). These findings are consistent with *in vitro* live imaging data and suggest that in KO microglia increased internalization of synaptic puncta at P12 is followed by more efficient degradation at P15. Overall, the loss of SHIP1 results in heightened phagocytic capacity and increased synapse elimination in cKO mice.

Synapse elimination by microglia is dependent on the complement system

Having found higher deposition of C1q in the hippocampus of cKO mice (Figures 4C–4F), we asked whether this increase was instrumental in mediating the enhanced synaptic pruning observed. To address this question, we constructed an adeno-associated virus (AAV) vector expressing CD55 under the control of the human Synapsin promoter. CD55 inhibits complement activation by suppressing the function of C3 and C5 convertases, thereby inhibiting both classical and alternative complement pathways.[54] We injected AAV-hSyn-CD55-p2A-mScarlet (CD55) or AAV-hSyn-mScarlet (mScarlet) into the ventricles of P0 or P1 control and cKO littermates. TAM was injected at P3 and P4, and brains were collected at P15 (Figure 6M). The mScarlet expression in the pyramidal neurons of the hippocampal CA1 confirmed the efficiency of the transduction and its localization in the soma as well as in dendrites and spines (Figures 6N, S6P, and S6Q). As expected, we observed a reduction of VGLUT1 in cKO mice injected with AAV-mScarlet compared with AAV-mScarlet controls. However, this decrease in cKO was prevented by AAV-CD55 injection, demonstrating that the synapse loss in cKO mice depends on the complement

system (Figures 6O and 6P). The overall C1q deposition in CD55-injected cKO mice did not differ from those in cKO injected with AAV-mScarlet, confirming that CD55 acts downstream of C1q (Figures S6R and S6S).

Synaptosome engulfment is enhanced in SHIP1 KO human iPSC-derived microglia

SNPs within *INPP5D* are strongly associated with AD risk.[2–4] Recent evidence suggests that SHIP1 AD-associated isoforms lack the phosphatase domain,[55] pointing to loss-of-function mechanisms. Therefore, we set out to functionally characterize human microglia lacking SHIP1 and investigated whether enhanced synapse elimination would be conserved. To this end, we used CRISPR-Cas9 to generate *INPP5D* homozygous knockout iPSC lines (Figures S7A–S7D). Using published protocols,[56,57] we differentiated SHIP1 KO iPSCs and their isogenic controls into iMG, which expressed the IBA1 marker (Figures 7A and 7B). We further confirmed by RNA-seq the downregulation of iPSC markers and induction of microglia markers in both SHIP1 WT (iMG control) and SHIP1 KO (iMG SHIP1) iMG (Figure 7C). In addition, principal component analysis (PCA) confirmed that the transcriptomic signature of our iMG was comparable to that of other iMG protocols and very distinct from the signature of iPSC and hematopoietic progenitors (HPCs), regardless of their genotype (Figure 7D). Efficient SHIP1 depletion was confirmed by WB and immunostaining of whole-cell lysates prepared from iMG SHIP1 compared with iMG control (Figure 7E). iMGs were exposed to synaptosomes isolated from human iPSC-derived neurons, prepared as previously described[58] and labeled with pHrodo (Figures S7E and S7F). Live imaging and quantification of the pHrodo signal showed an increase over time, which was abolished by the treatment with bafilomycin and cytochalasin D, confirming the specificity of the signal (Figure S7G). Quantitative analysis revealed that SHIP1 iMG engulfed more synaptosomes than control over time (Figures 7F and 7G; Videos S3 and S4). Overall, these findings further support the key role of SHIP1 in controlling microglia-mediated synapse elimination and indicate that this regulation is conserved across species.

Adult cKO mice display impaired cognitive function only if microglial SHIP1 is depleted early in development

Finally, we set out to investigate the functional consequences of SHIP1 KO-induced microglial dysfunction on mouse behavior, conducting a series of tests in adult mice that underwent *Inpp5d* deletion at P3 and P4 (Figure 7H). General locomotion and exploratory behavior did not differ between control and cKO

(C) Heatmap showing the expression of marker genes enriched in each cluster.

(D) Volcano plot showing DEGs in the aggregated cluster of excitatory hippocampal neurons based on MAST analysis; FDR adjusted *p* value < 0.05.

(E–G) (E) Overrepresented synaptic biological processes in cKO-upregulated DEGs using SynGO. Heatmap depicting the (F) net interaction strength and (G) net number of interactions predicted by CellChat between identified cell types in the cKO and control groups. Blue color indicates a relative decrease in cKO, while red indicates a relative increase in cKO.

(H) Net microglial signaling changes as predicted by CellChat, with positive values corresponding to enrichment in cKO and negative values corresponding to enrichment in control. Representation of the pathways for which microglia are the source (x axis) or the target (y axis).

(I) Relative differences between control and cKO in predicted signaling pathways from microglia targeting other cell types, as predicted by CellChat.

(J) Overview of signaling pathways from microglia that are relatively decreased in the cKO group, with predicted target cells shown on the x axis. Only cell types for which interactions were detected are depicted.

(K) Net excitatory hippocampal neuron signaling changes as predicted by CellChat, with positive values corresponding to enrichment in cKO and negative values corresponding to enrichment in control. Representation of the pathways for which neurons are the source (x axis) or the target (y axis).

(legend on next page)

Immunity
Article

CellPress
OPEN ACCESS
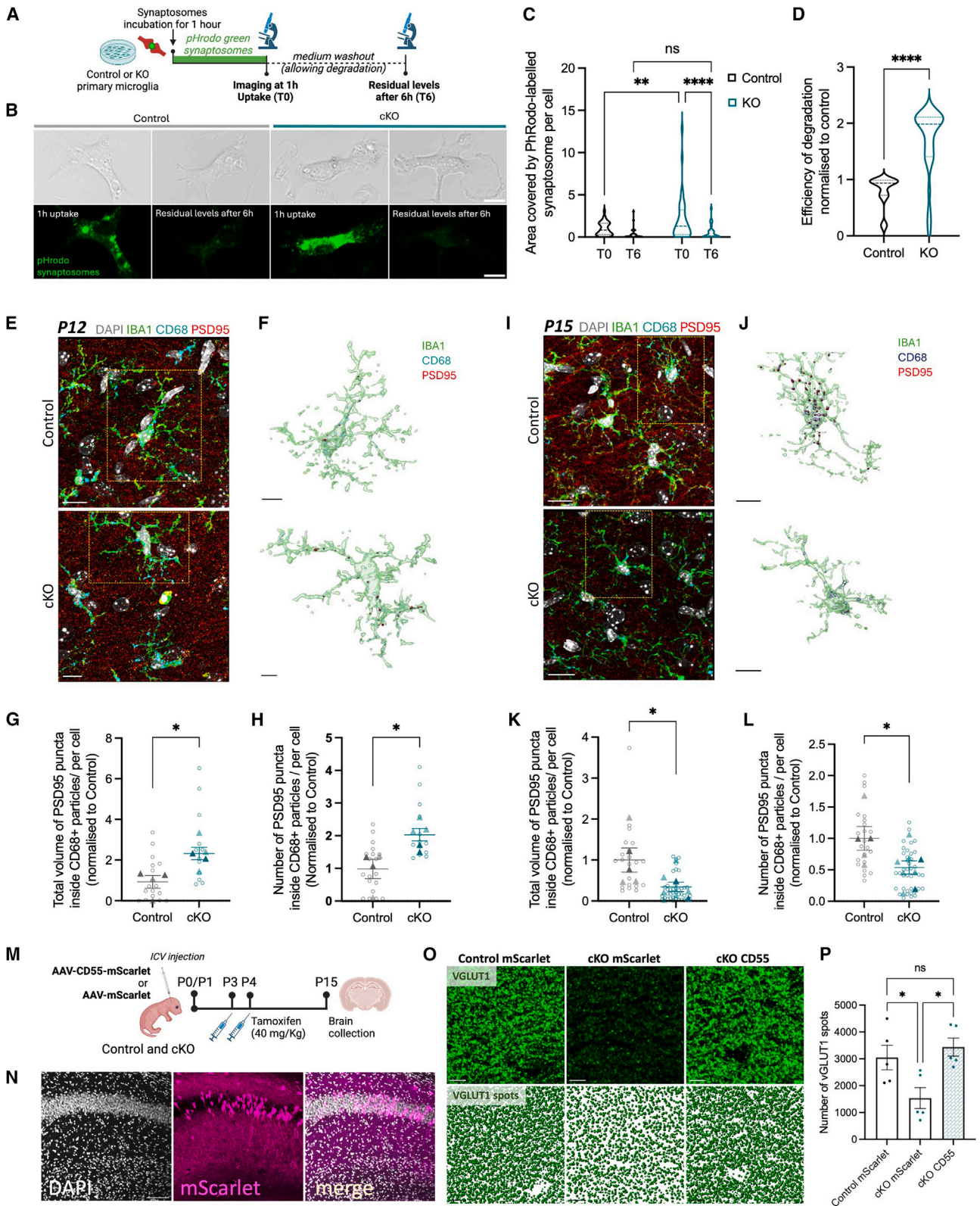
mice, as evidenced by the open field test (Figures 7I and 7J). In the novel object recognition task (NORT), cKO mice were unable to discriminate the novel object from the familiar one (Figure 7K), despite spending a similar amount of time exploring the objects as their control littermates during training (Figure S7H). Next, we exposed the mice to the Barnes maze to assess their spatial memory. On the second day of training, cKO mice took significantly longer than controls to locate the escape box, indicating delayed learning (Figure 7L), yet being successful in completing the test, as indicated by a similar time spent in the target quadrant (Figure 7M). No differences were observed in working memory and motor behavior, as supported by the Y-maze and the rotarod test (Figures S7I and S7J). These findings indicate that cKO mice display cognitive defects related to both episodic and spatial memory, despite no major alterations in the content of synaptic markers in the adult hippocampus (Figures S7L–S7S). Finally, we asked whether microglial SHIP1 is constitutively required for supporting cognitive function throughout life or whether its role is particularly relevant in circuit refinement at early postnatal stages. To address this question, we induced *Inpp5d* deletion in 3-month-old mice and tested them for cognitive behavior 1 month later (Figure 7N). This cohort of mice failed to show any episodic or spatial memory defects, as supported by their successful performance in both the NORT (Figure 7O) and the Barnes maze test (Figures 7P and S7K). These findings show that the loss of microglial SHIP1 early postnatally has long-lasting effects on adult cognitive behavior. However, its loss of function at later stages does not seem to have any impact, at least in the absence of additional pathologies. Overall, this study provides evidence that microglial SHIP1 is important for synapse remodeling and emphasizes the importance of developmentally critical windows for microglial risk genes to influence brain functioning.

DISCUSSION

INPP5D is one of the top risk genes for developing AD, and it is mainly expressed in microglia in the CNS. This study focuses on its role in modulating microglial function, during the early stages of brain development. Here, we show that not only SHIP1 is up-regulated in microglia associated with Aβ plaques in a mouse model of AD, confirming previous reports,[20,21] but it is also expressed during early brain development. A growing body of literature indicates that the molecular mechanisms crucial for brain development, such as synaptic pruning, are often reactivated during aging and neurodegenerative conditions. These mechanisms include the complement system and the TREM2 receptor.[39,40,51,62,63] The expression of these genes is often dynamic, peaking during brain development, decreasing in adult homeostatic microglia, and then increasing again in the case of brain diseases. The complement cascade is a good example of this biphasic behavior, with complement molecules being increased during development and in the brain and cerebrospinal fluid (CSF) from AD patients and in preclinical models.[1,38,39,62,64,65] We discovered that SHIP1 in the hippocampus follows a similar trajectory, supporting the important function of this protein in development. We also observed an unexpected regulation of *Inpp5d* mRNA-protein ratio depending on the brain structure analyzed, with transcripts remaining high in cortical areas and not correlating with protein abundance. The reduction of SHIP1 expression in the healthy adult hippocampus may provide vulnerability in a brain structure highly associated with cognitive decline in neurodegeneration.[66,67] Further investigations are needed to elucidate the underlying mechanisms.

Cytoplasmic SHIP1 is recruited via its SH2 domain to phosphorylated tyrosine residues at ITAM and ITIM motifs contained in adaptor molecules such as DAP12 or in FcRγ and C-type lectin receptors (CLRs), which have ITAMs as an integral component of their cytoplasmic tail, including CLEC7A.[8,68] DAP12, encoded by the *Tyrobp* gene, is a key downstream signaling molecule for surface receptors activity, such as TREM2 and C3R, mediating microglial migration and phagocytosis.[69] Thus, SHIP1 recruitment to the plasma membrane masks the docking site on ITAMs, preventing the binding of the SYK kinase effector, and therefore acts as a negative regulator of receptor activity. Additionally, once recruited to the plasma membrane, SHIP1 hydrolyzes PI(3,4,5)P3 to produce PI(3,4)P2. As a consequence, loss of SHIP1 would both exacerbate surface receptor activity and facilitate PI(3,4,5)P3 availability for downstream phosphatidylinositol 3-kinase (PI3K)/AKT signaling.[8,20,70]

Figure 6. SHIP1 cKO mice exhibit abnormal microglial synaptic pruning dependent on complement
(A) Experimental paradigm of pHrodo-labeled-synaptosome assay in primary microglia.
(B) Confocal z stack projections of primary SHIP1 KO and control microglia, incubated with pHrodo-labeled synaptosomes: 1 h uptake (T0) and after 6 h (T6). Scale bar: 10 μm.
(C) Relative quantification of area covered by pHrodo per cell; two-way ANOVA, Tukey's multiple comparison test: **$p < 0.01$, ****$p < 0.0001$.
(D–L) (D) Efficiency of degradation normalized to control; unpaired t test, ****$p < 0.0001$. T0: control $n = 34$ cells, KO $n = 36$ cells. T6: control $n = 32$ cells, KO $n = 30$ cells. Data are averaged from $N = 3$ independent experiments ($N = 3$ control and $N = 4$ KO-independent primary microglia isolations). Confocal z stack projections and 3D reconstruction of IBA1 surface and microglial engulfed PSD95 inside CD68+ structures, in P12 (E and F) and P15 (I and J) control and SHIP1 cKO mice. Reconstructed cells are highlighted in yellow. Scale bar: 10 μm in (E) and (I) and 8 μm in (F) and (J). Quantification of microglial engulfment, showing volume and number of PSD95-positive particles per microglial cell at P12 (G and H) and P15 (K and L). P12: $n = 19$ control cells vs. $n = 13$ cKO cells, reconstructed from $N = 4$ control vs. $N = 5$ cKO mice; unpaired t test, *$p < 0.05$. P15: $n = 22$ control cells vs. $n = 39$ cKO cells, reconstructed from $N = 5$ control vs. $N = 8$ cKO mice; unpaired t test, *$p < 0.05$.
(M) Experimental paradigm of either AAV-mScarlet or AAV-CD55-p2A-mScarlet intraventricular injections in P0/P1 control and cKO mice.
(N) Confocal z stack projections showing mScarlet expression in CA1 hippocampal neurons at P15. Scale bar: 50 μm.
(O) Confocal z stack projections and relative 3D spot reconstruction of VGLUT1 puncta in the hippocampal CA1 of control mice injected with AAV-mScarlet and cKO mice either injected with AAV-mScarlet or AAV-CD55-mScarlet.
(P) Quantification of VGLUT1 spot number, $N = 5$ control mScarlet, $N = 5$ SHIP1 cKO mScarlet, $N = 5$ SHIP1 cKO CD55-mScarlet; one-way ANOVA, Tukey's multiple comparisons test, *$p < 0.05$.
Animals are represented with triangles, whereas cells with circles. Females are indicated in light and males in dark colors. Multiple sections have been analyzed over independent experiments. Statistics are performed on animals.
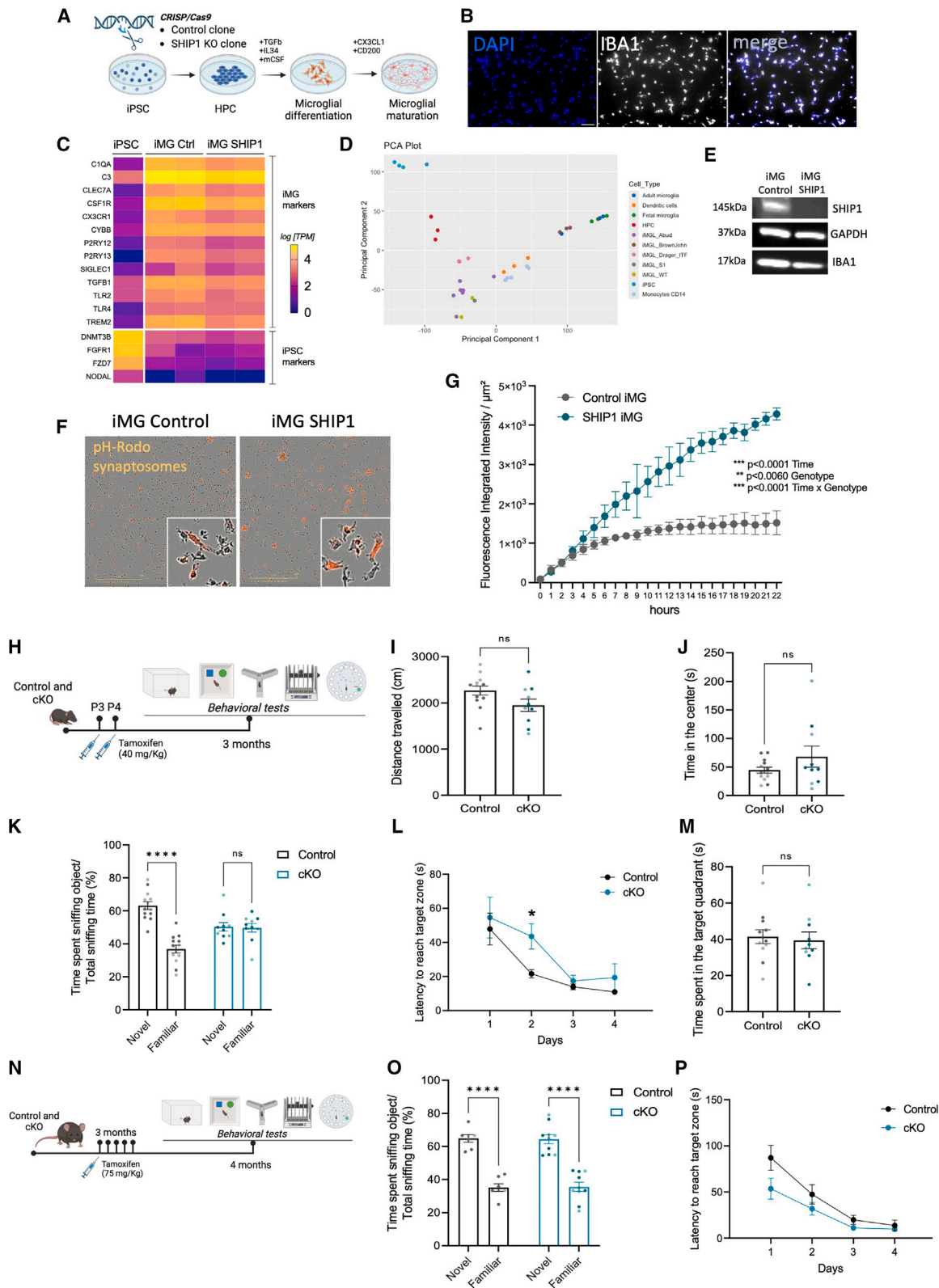
Figure 7. SHIP1 regulates synaptosomes engulfment in iMG and influences behavior in mice when depleted in early development

(A) Representative timeline for human iPSC CRISPR-Cas9 genome editing and subsequent microglia (iMG) differentiation.

(B) Representative acquisition of iMG stained for DAPI and IBA1.

In this study, we induced the cKO at P3 and P4 and found that at P15 acutely isolated microglia lacking SHIP1 exhibit a transcriptional signature characterized by increased expression of *Cd11c*, *Clec7a*, *Csf1*, *Cd63*, *Ccl3*, and *Ccl6*, among others, associated with reactive microglial states in both pathology and early development.[16–18,28,29,30,32] These findings align with recent studies showing a DAM-like phenotype in SHIP1 KO microglia from AD mice,[33,37,71] with the key difference being that, in this study, no amyloid pathology is involved and that microglial cells are isolated from the healthy developing hippocampus. It is important to note that several of the genes upregulated in our dataset are enriched in the disease-associated signature that requires TREM2 for progression.[28,29,72] GO analysis of our RNA-seq data revealed an enrichment in the regulation of tau kinase activity, underlying a possible link between the loss of SHIP1 and tau biology. In line with this, a recent study investigating the role of SHIP1-TREM2 interaction in an AD mouse model suggests that SHIP1 acts downstream of TREM2/DAP12 to regulate Aβ compaction and limit tau pathology.[20] Further studies are needed to investigate the microglial TREM2-SHIP1 axis and its interaction with tau in brain development.

Functionally, we observed that the loss of SHIP1 resulted in increased phagocytosis of both Aβ and synaptosomes, indicating a general enhancement in the phagocytic capacity, accounted by both engulfment and degradation. This is in line with recent reports that show enhanced amyloid engulfment by SHIP1 KO microglia, both *in vitro* and *in vivo*.[33,37]

In our cKO mouse model, the C1q complement, a well-known eat-me signal for synapses,[38–40] is abnormally upregulated; however, the underlying mechanism remains to be elucidated. We found that the increase in complement was associated with increased synaptic engulfment at P12, as indicated by the higher content of PSD95-positive material within KO microglia. We also found that a few days later, at P15, the synaptic puncta contained by microglia were substantially reduced, as was the overall synaptic density. These findings may suggest an increased efficiency in both engulfment and degradation by microglia *in vivo*, as we have observed *in vitro*, leading to a faster elimination of the synaptic content within the cells. This interpre-

tation presupposes that the amount of engulfed synaptic structures progressively decreases across the time window that we have assessed, while the degradation efficiently continues. Consistent with this possibility, in the healthy developing brain, the process of microglia-mediated synapse elimination has been shown to peak over a few day.[73] Alternatively, it cannot be excluded that the decreased synaptic content seen within microglia at P15 in cKO mice may be contributed by the overall reduction in synaptic structures available for engulfment and elimination. Finally, it may also be possible that the loss of SHIP1 in microglia simply accelerates the window of synaptic pruning and that the two snapshots at P12 and P15 may not be sufficient to recapitulate the entire process. While our data emphasize the importance of introducing two different time points when investigating the dynamics of microglia-mediated synapse elimination *in vivo*, we acknowledge that further experiments are required to corroborate these observations.

Abnormal pruning led to a significant reduction in synapse density in the hippocampal CA1 region at P15, as shown by decreased number of apposed VGLUT1-PSD95 puncta. It is important to note that VGLUT1 synaptic changes were only present in the hippocampal CA1 region, with no differences detected between control and cKO littermates in the CA3 area. Conversely, a general decrease in PSD95 was observed in both the hippocampal CA1 and CA3 structures, as further confirmed by WB analysis. These findings highlight the heterogeneity and complexity of the microglia-mediated synaptic phenotype overall and are consistent with previous research that has identified a CA1-specific phenotype in TREM2 KO mice.[51,74] Importantly, we showed that synapse loss in cKO mice could be prevented by overexpression of the decay accelerating factor DAF (CD55), proving that the complement system is a key player in SHIP1-dependent synapse regulation. Complement has emerged as an important player also in the early stages of AD, mediating pathological synaptic pruning by microglia and driving the formation of the lytic membrane attack complex (MAC) to directly damage synapses.[75,76] Therefore, further investigations on the role of complement in adult SHIP1 cKO are warranted.

Bioinformatic analysis of snRNA-seq data from the entire hippocampus predicted a decrease in synaptic strength among both excitatory and inhibitory neurons in cKO mice, consistent with the documented reduction in functional synaptic structures. The analysis also showed an increase in the predicted number of neuron-neuron interactions in cKO mice, suggesting a potential compensatory mechanism to counterbalance the loss of synapses. This interpretation aligns with the lack of differences measured by whole-cell recordings at P15, including both the amplitude and frequency of excitatory postsynaptic currents.

Different SNPs have been identified in *INPP5D*, some of which are protective while others increase the risk for AD.[55,77] Reports from autopsies of AD cases suggest that SHIP1 expression increases in association with Aβ deposits.[21] However, recent studies have shown that soluble full-length SHIP1 in AD brains is reduced compared with cognitively normal controls.[55,78] In addition, some *INPP5D* risk variants associated with AD have been reported to lack the phosphatase domain,[6,55] thus supporting SHIP1 loss-of-function mechanisms in pathological contexts. Significant reductions in steady-state SHIP1 protein expression have also been observed in a significant percentage of inflammatory bowel disease (IBD) patients, particularly those with severe disease.[79] Taken together, these findings highlight the significant regulation of SHIP1 in pathological conditions, although the exact functional outcomes of its dysregulation are still poorly understood. Using CRISPR-Cas9-engineered human iPSC lines, we were able to demonstrate that enhanced engulfment of synaptic structures is also present in SHIP1 KO iMG. This adds to the significance of our findings, indicating that similar mechanisms are conserved in humans.

Aberrant synapse remodeling by microglia has often been linked to long-lasting behavioral consequences.[51,53,80] We found that SHIP1 cKO adult mice displayed impaired object recognition and spatial learning, which are strongly linked to hippocampal function.[81–83] It is important to note, however, that the loss of microglial SHIP1 was critical for adult cognitive function only when it occurred at early postnatal stages. SHIP1 KO produced no effects when induced after development. Our findings that SHIP1 protein expression is substantially reduced in the healthy adult brain could explain this apparent discrepancy. It is also important to emphasize that the defective synaptic density observed at P15 was normalized in adult mice, consistent with the work of Castranio et al.,[37] showing comparable amount of PSD95 and synaptophysin in the brains of adult cKO mice crossed with 5xFAD.[37] Recent studies using preclinical models have increased our understanding of how SHIP1 could influence AD pathology, including evidence of increased phagocytic capacity toward Aβ by microglia lacking SHIP1.[33,37,71] Furthermore, haploinsufficiency in 5xFAD mice rescued working memory defects,[71] suggesting a beneficial effect of SHIP1 reduction in the AD context. Nevertheless, we could speculate that the increase in SHIP1 observed in association with plaques may reflect, at least in the initial stages of the pathology, a targeted response aimed at regulating phagocytosis, which—if prolonged—is likely to contribute to the defective clearance capacity of microglia typically observed in late-onset AD.

Pharmacological inhibition of SHIP1 has been shown to promote the engulfment of Aβ and apoptotic neurons as well as modulate lysosomal content.[57] On the other hand, specific ago-

nism of SHIP1 phosphatase activity results in increased intracellular degradation of lipid-laden cargoes while leaving their uptake unaltered.[36] Additionally, SHIP1 has been identified as a critical regulator of inflammatory response and inflammasome activation, adding to the complexity of its various functions.[6,84] This aspect should be carefully considered, as the Cx3cr1[creErt2] reporter mouse line we used in this study targets not only microglia but also other immune cells, which can respond by increasing proinflammatory molecules.[85,86] These findings suggest that SHIP1 regulation is complex and may require fine-tuned modulation to effectively control phagocytosis and inflammation.[87] Understanding the underlying molecular mechanisms will be crucial in developing new approaches to target microglia in neurodegeneration. However, despite a growing interest in the role of SHIP1 in AD,[20,21,33,37,55,71] its physiological functions in the healthy brain, particularly during development, remained poorly investigated. Overall, our findings reveal a role for the AD risk gene *INPP5D* in controlling microglia-mediated synapse refinement in the early postnatal brain in a complement-dependent manner. Microglial SHIP1 cKO-dependent miswiring of the brain leads to long-lasting consequences on cognitive function and may provide a link to vulnerability to neurodegeneration.

Limitations of the study

While this study uncovers a role for SHIP1 in microglia-mediated synaptic refinement during brain development through the complement system, it does not provide insights into the underlying molecular mechanisms. What drives the complement upregulation when microglial SHIP1 is deleted remains unclear and requires additional experimental work. Furthermore, the molecular signals that control the developmentally regulated reduction of SHIP1 are not understood. Whether microglial overexpression of SHIP1 in brain development would result in a phenotype opposite to the one induced by the loss of function remains to be investigated. Finally, the broad consequences of microglial SHIP1 depletion on other glial cells in the hippocampus, such as astrocytes and oligodendrocytes, have only been predicted by bioinformatic approaches and not further investigated. It would be important in the future to deepen these studies by assessing in detail how SHIP1 may influence the crosstalk of microglia with other cells in the brain.

RESOURCE AVAILABILITY

Lead contact

Further information and requests for resources should be directed to and will be fulfilled by the lead contact, Rosa C. Paolicelli (rosachiara.paolicelli@unil.ch).

Materials availability

All reagents generated in this study are available upon reasonable request to the lead contact.

Data and code availability

- The mouse microglia bulk RNA-seq data (GEO: GSE268277), the mouse snRNA-seq data (GEO: GSE264452), and the human iPSC-derived microglia RNA-seq data (GEO: GSE279176) have been deposited on Gene Expression Omnibus (GEO) public functional genomics data repository. Mouse proteomics data (PRIDE: PXD052118) have been deposited on Proteomics Identification Database (PRIDE).

CellPress
OPEN ACCESS

- This paper does not report original code.
- Codes used for snRNA-seq data analysis are accessible at: https://github.com/jmkotah/SHIP1_snRNASeq_analysis.
- Any additional information required to reanalyze the data reported in this paper is available from the lead contact upon request.

AUTHOR CONTRIBUTIONS

A.M. and A.-C.C. designed, performed, analyzed, and interpreted most experiments and co-edited the manuscript. C.P., J.M.K., K.M., L.L., G.L., M.P., T.L.W., S.G.M., and W.G.K. designed and performed some experiments. A.I. and J.M.K. performed bioinformatic analysis on mouse samples. C.P. performed the bioinformatic analysis on human microglia samples. D.B., V.M.-A., N.I., A.S., S.G.M., A.M.G., B.J.L.E., W.G.K., and R.C.P. supervised experiments. R.C.P. developed the concept; designed, performed, analyzed, and interpreted experiments; and wrote the manuscript. All authors read the manuscript and provided comments.

DECLARATION OF INTERESTS

A.M.G. serves on the SRB of Genentech and the SAB of Muna Therapeutics. A.M.G. received funding from JPB Foundation and NIH U01AG058635. W.G.K. and C.P. have a patent pending regarding the use of human iPSCs that have been gene edited at the SHIP1/INPP5D locus for use as a cell therapy in dementias.

STAR★METHODS

Detailed methods are provided in the online version of this paper and include the following:

- KEY RESOURCES TABLE
- EXPERIMENTAL MODEL AND STUDY PARTICIPANT DETAILS
  - Animals
  - Cell lines and primary cultures
  - Generation of human INPP5D knockout iPSC lines
  - hiPSC differentiation into microglia (iMG)
- METHOD DETAILS
  - Animal perfusion and brain slicing
  - Acute isolation of microglia
  - Phagocytic assays in primary microglia
  - Western blot
  - ELISA immunoassays
  - Immunofluorescence staining
  - Confocal microscopy and imaging analysis
  - RNA extraction, retrotranscription and RT-qPCR
  - Bulk RNAseq analysis of mouse microglia
  - RNA-seq analysis of mouse microglia
  - Single nuclei RNA sequencing of mouse hippocampi
  - Single nuclei RNASeq data analysis
  - Excitatory Neurons (Snap25+/Gad1-/Gad2-)
  - Proteomics
  - Intracerebroventricular injection of AAV
  - Electrophysiological recordings of CA1 pyramidal neurons
  - Genomic integrity of human iPSC lines
  - hiPSC genomic stability assay
  - EVs isolation from BV2
  - Behavioral testing
- QUANTIFICATION AND STATISTICAL ANALYSIS

SUPPLEMENTAL INFORMATION

Supplemental information can be found online at https://doi.org/10.1016/j.immuni.2024.11.003.

REFERENCES

1. Bellenguez, C., Küçükali, F., Jansen, I.E., Kleineidam, L., Moreno-Grau, S., Amin, N., Naj, A.C., Campos-Martin, R., Grenier-Boley, B., Andrade, V., et al. (2022). New insights into the genetic etiology of Alzheimer's disease and related dementias. Nat. Genet. 54, 412–436. https://doi.org/10.1038/s41588-022-01024-z.

2. Kunkle, B.W., Grenier-Boley, B., Sims, R., Bis, J.C., Damotte, V., Naj, A.C., Boland, A., Vronskaya, M., van der Lee, S.J., Amlie-Wolf, A., et al. (2019). Genetic meta-analysis of diagnosed Alzheimer's disease identifies new risk loci and implicates Abeta, tau, immunity and lipid processing. Nat. Genet. 51, 414–430. https://doi.org/10.1038/s41588-019-0358-2.

3. Lambert, J.C., Ibrahim-Verbaas, C.A., Harold, D., Naj, A.C., Sims, R., Bellenguez, C., DeStafano, A.L., Bis, J.C., Beecham, G.W., Grenier-Boley, B., et al. (2013). Meta-analysis of 74,046 individuals identifies 11 new susceptibility loci for Alzheimer's disease. Nat. Genet. 45, 1452–1458. https://doi.org/10.1038/ng.2802.

4. Wightman, D.P., Jansen, I.E., Savage, J.E., Shadrin, A.A., Bahrami, S., Holland, D., Rongve, A., Børte, S., Winsvold, B.S., Drange, O.K., et al. (2021). A genome-wide association study with 1,126,563 individuals identifies new risk loci for Alzheimer's disease. Nat. Genet. 53, 1276–1282. https://doi.org/10.1038/s41588-021-00921-z.

5. Zhang, Y., Chen, K., Sloan, S.A., Bennett, M.L., Scholze, A.R., O'Keeffe, S., Phatnani, H.P., Guarnieri, P., Caneda, C., Ruderisch, N., et al. (2014). An RNA-sequencing transcriptome and splicing database of glia, neurons, and vascular cells of the cerebral cortex. J. Neurosci. 34, 11929–11947. https://doi.org/10.1523/JNEUROSCI.1860-14.2014.

6. Chou, V., Pearse, R.V., 2nd, Aylward, A.J., Ashour, N., Taga, M., Terzioglu, G., Fujita, M., Fancher, S.B., Sigalov, A., Benoit, C.R., et al. (2023). INPP5D regulates inflammasome activation in human microglia. Nat. Commun. 14, 7552. https://doi.org/10.1038/s41467-023-42819-w.

7. Ooms, L.M., Horan, K.A., Rahman, P., Seaton, G., Gurung, R., Kethesparan, D.S., and Mitchell, C.A. (2009). The role of the inositol polyphosphate 5-phosphatases in cellular function and human disease. Biochem. J. 419, 29–49. https://doi.org/10.1042/BJ20081673.

8. Peng, Q., Malhotra, S., Torchia, J.A., Kerr, W.G., Coggeshall, K.M., and Humphrey, M.B. (2010). TREM2- and DAP12-dependent activation of PI3K requires DAP10 and is inhibited by SHIP1. Sci. Signal. 3, ra38. https://doi.org/10.1126/scisignal.2000500.

9. Gillooly, D.J., Simonsen, A., and Stenmark, H. (2001). Phosphoinositides and phagocytosis. J. Cell Biol. *155*, 15–17. https://doi.org/10.1083/jcb.200109001.

10. Di Paolo, G., and De Camilli, P. (2006). Phosphoinositides in cell regulation and membrane dynamics. Nature *443*, 651–657. https://doi.org/10.1038/nature05185.

11. Mócsai, A., Ruland, J., and Tybulewicz, V.L.J. (2010). The SYK tyrosine kinase: a crucial player in diverse biological functions. Nat. Rev. Immunol. *10*, 387–402. https://doi.org/10.1038/nri2765.

12. Long, J.M., and Holtzman, D.M. (2019). Alzheimer Disease: An Update on Pathobiology and Treatment Strategies. Cell *179*, 312–339.

13. Gjoneska, E., Pfenning, A.R., Mathys, H., Quon, G., Kundaje, A., Tsai, L.H., and Kellis, M. (2015). Conserved epigenomic signals in mice and humans reveal immune basis of Alzheimer's disease. Nature *518*, 365–369. https://doi.org/10.1038/nature14252.

14. Gosselin, D., Skola, D., Coufal, N.G., Holtman, I.R., Schlachetzki, J.C.M., Sajti, E., Jaeger, B.N., O'Connor, C., Fitzpatrick, C., Pasillas, M.P., et al. (2017). An environment-dependent transcriptional network specifies human microglia identity. Science *356*, eaal3222. https://doi.org/10.1126/science.aal3222.

15. Nott, A., Holtman, I.R., Coufal, N.G., Schlachetzki, J.C.M., Yu, M., Hu, R., Han, C.Z., Pena, M., Xiao, J., Wu, Y., et al. (2019). Brain cell type-specific enhancer-promoter interactome maps and disease-risk association. Science *366*, 1134–1139. https://doi.org/10.1126/science.aay0793.

16. Hammond, T.R., Dufort, C., Dissing-Olesen, L., Giera, S., Young, A., Wysoker, A., Walker, A.J., Gergits, F., Segel, M., Nemesh, J., et al. (2019). Single-Cell RNA Sequencing of Microglia throughout the Mouse Lifespan and in the Injured Brain Reveals Complex Cell-State Changes. Immunity *50*, 253–271.e6. https://doi.org/10.1016/j.immuni.2018.11.004.

17. Li, Q., Cheng, Z., Zhou, L., Darmanis, S., Neff, N.F., Okamoto, J., Gulati, G., Bennett, M.L., Sun, L.O., Clarke, L.E., et al. (2019). Developmental Heterogeneity of Microglia and Brain Myeloid Cells Revealed by Deep Single-Cell RNA Sequencing. Neuron *101*, 207–223.e10. https://doi.org/10.1016/j.neuron.2018.12.006.

18. Masuda, T., Sankowski, R., Staszewski, O., Böttcher, C., Amann, L., Sagar, S., Scheiwe, C., Nessler, S., Kunz, P., van Loo, G., et al. (2019). Spatial and temporal heterogeneity of mouse and human microglia at single-cell resolution. Nature *566*, 388–392. https://doi.org/10.1038/s41586-019-0924-x.

19. Kracht, L., Borggrewe, M., Eskandar, S., Brouwer, N., Chuva de Sousa Lopes, S.M., Laman, J.D., Scherjon, S.A., Prins, J.R., Kooistra, S.M., and Eggen, B.J.L. (2020). Human fetal microglia acquire homeostatic immune-sensing properties early in development. Science *369*, 530–537. https://doi.org/10.1126/science.aba5906.

20. Iguchi, A., Takatori, S., Kimura, S., Muneto, H., Wang, K., Etani, H., Ito, G., Sato, H., Hori, Y., Sasaki, J., et al. (2023). INPP5D modulates TREM2 loss-of-function phenotypes in a beta-amyloidosis mouse model. iScience. iScience *26*, 106375. https://doi.org/10.1016/j.isci.2023.106375.

21. Tsai, A.P., Lin, P.B.C., Dong, C., Moutinho, M., Casali, B.T., Liu, Y., Lamb, B.T., Landreth, G.E., Oblak, A.L., and Nho, K. (2021). INPP5D expression is associated with risk for Alzheimer's disease and induced by plaque-associated microglia. Neurobiol. Dis. *153*, 105303. https://doi.org/10.1016/j.nbd.2021.105303.

22. Knobloch, M., Konietzko, U., Krebs, D.C., and Nitsch, R.M. (2007). Intracellular Abeta and cognitive deficits precede beta-amyloid deposition in transgenic arcAbeta mice. Neurobiol. Aging *28*, 1297–1306. https://doi.org/10.1016/j.neurobiolaging.2006.06.019.

23. Paolicelli, R.C., Sierra, A., Stevens, B., Tremblay, M.E., Aguzzi, A., Ajami, B., Amit, I., Audinat, E., Bechmann, I., Bennett, M., et al. (2022). Microglia states and nomenclature: A field at its crossroads. Neuron *110*, 3458–3483. https://doi.org/10.1016/j.neuron.2022.10.020.

24. Pinto, A.R., Paolicelli, R., Salimova, E., Gospocic, J., Slonimsky, E., Bilbao-Cortes, D., Godwin, J.W., and Rosenthal, N.A. (2012). An abun-

dant tissue macrophage population in the adult murine heart with a distinct alternatively-activated macrophage profile. PLoS One *7*, e36814. https://doi.org/10.1371/journal.pone.0036814.

25. Parkhurst, C.N., Yang, G., Ninan, I., Savas, J.N., Yates, J.R., 3rd, Lafaille, J.J., Hempstead, B.L., Littman, D.R., and Gan, W.B. (2013). Microglia promote learning-dependent synapse formation through brain-derived neurotrophic factor. Cell *155*, 1596–1609. https://doi.org/10.1016/j.cell.2013.11.030.

26. Wang, J.W., Howson, J.M., Ghansah, T., Desponts, C., Ninos, J.M., May, S.L., Nguyen, K.H.T., Toyama-Sorimachi, N., and Kerr, W.G. (2002). Influence of SHIP on the NK repertoire and allogeneic bone marrow transplantation. Science *295*, 2094–2097. https://doi.org/10.1126/science.1068438.

27. Zyla, J., Marczyk, M., Domaszewska, T., Kaufmann, S.H.E., Polanska, J., and Weiner, J. (2019). Gene set enrichment for reproducible science: comparison of CERNO and eight other algorithms. Bioinformatics *35*, 5146–5154. https://doi.org/10.1093/bioinformatics/btz447.

28. Keren-Shaul, H., Spinrad, A., Weiner, A., Matcovitch-Natan, O., Dvir-Szternfeld, R., Ulland, T.K., David, E., Baruch, K., Lara-Astaiso, D., Toth, B., et al. (2017). A Unique Microglia Type Associated with Restricting Development of Alzheimer's Disease. Cell *169*, 1276–1290.e17. https://doi.org/10.1016/j.cell.2017.05.018.

29. Krasemann, S., Madore, C., Cialic, R., Baufeld, C., Calcagno, N., El Fatimy, R., Beckers, L., O'Loughlin, E., Xu, Y., Fanek, Z., et al. (2017). The TREM2-APOE Pathway Drives the Transcriptional Phenotype of Dysfunctional Microglia in Neurodegenerative Diseases. Immunity *47*, 566–581.e9. https://doi.org/10.1016/j.immuni.2017.08.008.

30. Sala Frigerio, C., Wolfs, L., Fattorelli, N., Thrupp, N., Voytyuk, I., Schmidt, I., Mancuso, R., Chen, W.T., Woodbury, M.E., Srivastava, G., et al. (2019). The Major Risk Factors for Alzheimer's Disease: Age, Sex, and Genes Modulate the Microglia Response to Abeta Plaques. Cell Rep. *27*, 1293–1306.e6. https://doi.org/10.1016/j.celrep.2019.03.099.

31. Gerrits, E., Brouwer, N., Kooistra, S.M., Woodbury, M.E., Vermeiren, Y., Lambourne, M., Mulder, J., Kummer, M., Möller, T., Biber, K., et al. (2021). Distinct amyloid-beta and tau-associated microglia profiles in Alzheimer's disease. Acta Neuropathol. *141*, 681–696. https://doi.org/10.1007/s00401-021-02263-w.

32. Lawrence, A.R., Canzi, A., Bridlance, C., Olivié, N., Lansonneur, C., Catale, C., Pizzamiglio, L., Kloeckner, B., Silvin, A., Munro, D.A.D., et al. (2024). Microglia maintain structural integrity during fetal brain morphogenesis. Cell *187*, 962–980.e19. https://doi.org/10.1016/j.cell.2024.01.012.

33. Samuels, J.D., Moore, K.A., Ennerfelt, H.E., Johnson, A.M., Walsh, A.E., Price, R.J., and Lukens, J.R. (2023). The Alzheimer's disease risk factor INPP5D restricts neuroprotective microglial responses in amyloid beta-mediated pathology. Alzheimers Dement. *19*, 4908–4921. https://doi.org/10.1002/alz.13089.

34. Welsh, J.A., Goberdhan, D.C.I., O'Driscoll, L., Buzas, E.I., Blenkiron, C., Bussolati, B., Cai, H., Di Vizio, D., Driedonks, T.A.P., Erdbrügger, U., et al. (2024). Minimal information for studies of extracellular vesicles (MISEV2023): From basic to advanced approaches. J. Extracell. Vesicles *13*, e12404. https://doi.org/10.1002/jev2.12404.

35. Hurwitz, S.N., Conlon, M.M., Rider, M.A., Brownstein, N.C., and Meckes, D.G., Jr. (2016). Nanoparticle analysis sheds budding insights into genetic drivers of extracellular vesicle biogenesis. J. Extracell. Vesicles *5*, 31295. https://doi.org/10.3402/jev.v5.31295.

36. Pedicone, C., Fernandes, S., Matera, A., Meyer, S.T., Loh, S., Ha, J.H., Bernard, D., Chisholm, J.D., Paolicelli, R.C., and Kerr, W.G. (2022). Discovery of a novel SHIP1 agonist that promotes degradation of lipid-laden phagocytic cargo by microglia. iScience *25*, 104170. https://doi.org/10.1016/j.isci.2022.104170.

37. Castranio, E.L., Hasel, P., Haure-Mirande, J.V., Ramirez Jimenez, A.V., Hamilton, B.W., Kim, R.D., Glabe, C.G., Wang, M., Zhang, B., Gandy, S., et al. (2023). Microglial INPP5D limits plaque formation and glial

Immunity
Article

CellPress
OPEN ACCESS

reactivity in the PSAPP mouse model of Alzheimer's disease. Alzheimers Dement. *19*, 2239–2252. https://doi.org/10.1002/alz.12821.

38. Dejanovic, B., Wu, T., Tsai, M.-C., Graykowski, D., Gandham, V.D., Rose, C.M., Bakalarski, C.E., Ngu, H., Wang, Y., Pandey, S., et al. (2022). Complement C1q-dependent excitatory and inhibitory synapse elimination by astrocytes and microglia in Alzheimer's disease mouse models. Nat. Aging *2*, 837–850. https://doi.org/10.1038/s43587-022-00281-1.

39. Hong, S., Beja-Glasser, V.F., Nfonoyim, B.M., Frouin, A., Li, S., Ramakrishnan, S., Merry, K.M., Shi, Q., Rosenthal, A., Barres, B.A., et al. (2016). Complement and microglia mediate early synapse loss in Alzheimer mouse models. Science *352*, 712–716. https://doi.org/10.1126/science.aad8373.

40. Schafer, D.P., Lehrman, E.K., Kautzman, A.G., Koyama, R., Mardinly, A.R., Yamasaki, R., Ransohoff, R.M., Greenberg, M.E., Barres, B.A., and Stevens, B. (2012). Microglia sculpt postnatal neural circuits in an activity and complement-dependent manner. Neuron *74*, 691–705. https://doi.org/10.1016/j.neuron.2012.03.026.

41. Koopmans, F., van Nierop, P., Andres-Alonso, M., Byrnes, A., Cijsouw, T., Coba, M.P., Cornelisse, L.N., Farrell, R.J., Goldschmidt, H.L., Howrigan, D.P., et al. (2019). SynGO: An Evidence-Based, Expert-Curated Knowledge Base for the Synapse. Neuron *103*, 217–234.e4. https://doi.org/10.1016/j.neuron.2019.05.002.

42. Jin, S., Guerrero-Juarez, C.F., Zhang, L., Chang, I., Ramos, R., Kuan, C.H., Myung, P., Plikus, M.V., and Nie, Q. (2021). Inference and analysis of cell-cell communication using CellChat. Nat. Commun. *12*, 1088. https://doi.org/10.1038/s41467-021-21246-9.

43. Chaudhury, A.R., Gerecke, K.M., Wyss, J.M., Morgan, D.G., Gordon, M.N., and Carroll, S.L. (2003). Neuregulin-1 and erbB4 immunoreactivity is associated with neuritic plaques in Alzheimer disease brain and in a transgenic model of Alzheimer disease. J. Neuropathol. Exp. Neurol. *62*, 42–54. https://doi.org/10.1093/jnen/62.1.42.

44. Borggrewe, M., Kooistra, S.M., Noelle, R.J., Eggen, B.J.L., and Laman, J.D. (2020). Exploring the VISTA of microglia: immune checkpoints in CNS inflammation. J. Mol. Med. (Berl.) *98*, 1415–1430. https://doi.org/10.1007/s00109-020-01968-x.

45. Südhof, T.C. (2017). Synaptic Neurexin Complexes: A Molecular Code for the Logic of Neural Circuits. Cell *171*, 745–769. https://doi.org/10.1016/j.cell.2017.10.024.

46. Matsukawa, H., Akiyoshi-Nishimura, S., Zhang, Q., Luján, R., Yamaguchi, K., Goto, H., Yaguchi, K., Hashikawa, T., Sano, C., Shigemoto, R., et al. (2014). Netrin-G/NGL complexes encode functional synaptic diversification. J. Neurosci. *34*, 15779–15792. https://doi.org/10.1523/JNEUROSCI.1141-14.2014.

47. Henderson, N.T., and Dalva, M.B. (2018). EphBs and ephrin-Bs: Trans-synaptic organizers of synapse development and function. Mol. Cell. Neurosci. *91*, 108–121. https://doi.org/10.1016/j.mcn.2018.07.002.

48. Sytnyk, V., Leshchyns'ka, I., and Schachner, M. (2017). Neural Cell Adhesion Molecules of the Immunoglobulin Superfamily Regulate Synapse Formation, Maintenance, and Function. Trends Neurosci. *40*, 295–308. https://doi.org/10.1016/j.tins.2017.03.003.

49. Jahncke, J.N., and Wright, K.M. (2023). The many roles of dystroglycan in nervous system development and function: Dystroglycan and neural circuit development: Dystroglycan and neural circuit development. Dev. Dyn. *252*, 61–80. https://doi.org/10.1002/dvdy.516.

50. Ding, X., Wang, J., Huang, M., Chen, Z., Liu, J., Zhang, Q., Zhang, C., Xiang, Y., Zen, K., and Li, L. (2021). Loss of microglial SIRPalpha promotes synaptic pruning in preclinical models of neurodegeneration. Nat. Commun. *12*, 2030. https://doi.org/10.1038/s41467-021-22301-1.

51. Filipello, F., Morini, R., Corradini, I., Zerbi, V., Canzi, A., Michalski, B., Erreni, M., Markicevic, M., Starvaggi-Cucuzza, C., Otero, K., et al. (2018). The Microglial Innate Immune Receptor TREM2 Is Required for Synapse Elimination and Normal Brain Connectivity. Immunity *48*, 979–991.e8. https://doi.org/10.1016/j.immuni.2018.04.016.

52. Paolicelli, R.C., Bolasco, G., Pagani, F., Maggi, L., Scianni, M., Panzanelli, P., Giustetto, M., Ferreira, T.A., Guiducci, E., Dumas, L.,

et al. (2011). Synaptic pruning by microglia is necessary for normal brain development. Science *333*, 1456–1458. https://doi.org/10.1126/science.1202529.

53. Zhan, Y., Paolicelli, R.C., Sforazzini, F., Weinhard, L., Bolasco, G., Pagani, F., Vyssotski, A.L., Bifone, A., Gozzi, A., Ragozzino, D., and Gross, C.T. (2014). Deficient neuron-microglia signaling results in impaired functional brain connectivity and social behavior. Nat. Neurosci. *17*, 400–406. https://doi.org/10.1038/nn.3641.

54. Nicholson-Weller, A., and Wang, C.E. (1994). Structure and function of decay accelerating factor CD55. J. Lab. Clin. Med. *123*, 485–491.

55. Zajac, D.J., Simpson, J., Zhang, E., Parikh, I., and Estus, S. (2023). Expression of INPP5D Isoforms in Human Brain: Impact of Alzheimer's Disease Neuropathology and Genetics. Genes (Basel) *14*, 763. https://doi.org/10.3390/genes14030763.

56. McQuade, A., Coburn, M., Tu, C.H., Hasselmann, J., Davtyan, H., and Blurton-Jones, M. (2018). Development and validation of a simplified method to generate human microglia from pluripotent stem cells. Mol. Neurodegener. *13*, 67. https://doi.org/10.1186/s13024-018-0297-x.

57. Pedicone, C., Fernandes, S., Dungan, O.M., Dormann, S.M., Viernes, D.R., Adhikari, A.A., Choi, L.B., De Jong, E.P., Chisholm, J.D., and Kerr, W.G. (2020). Pan-SHIP1/2 inhibitors promote microglia effector functions essential for CNS homeostasis. J. Cell Sci. *133*, jcs238030. https://doi.org/10.1242/jcs.238030.

58. Bowles, K.R., Pugh, D.A., Pedicone, C., Oja, L., Weitzman, S.A., Liu, Y., Chen, J.L., Disney, M.D., and Goate, A.M. (2023). Development of MAPT S305 mutation models exhibiting elevated 4R tau expression, resulting in altered neuronal and astrocytic function. Preprint at bioRxiv. https://doi.org/10.1101/2023.06.02.543224.

59. Dräger, N.M., Sattler, S.M., Huang, C.T.L., Teter, O.M., Leng, K., Hashemi, S.H., Hong, J., Aviles, G., Clelland, C.D., Zhan, L., et al. (2022). A CRISPRi/a platform in human iPSC-derived microglia uncovers regulators of disease states. Nat. Neurosci. *25*, 1149–1162. https://doi.org/10.1038/s41593-022-01131-4.

60. Abud, E.M., Ramirez, R.N., Martinez, E.S., Healy, L.M., Nguyen, C.H.H., Newman, S.A., Yeromin, A.V., Scarfone, V.M., Marsh, S.E., Fimbres, C., et al. (2017). iPSC-Derived Human Microglia-like Cells to Study Neurological Diseases. Neuron *94*, 278–293.e9. https://doi.org/10.1016/j.neuron.2017.03.042.

61. Brownjohn, P.W., Smith, J., Solanki, R., Lohmann, E., Houlden, H., Hardy, J., Dietmann, S., and Livesey, F.J. (2018). Functional Studies of Missense TREM2 Mutations in Human Stem Cell-Derived Microglia. Stem Cell Rep. *10*, 1294–1307. https://doi.org/10.1016/j.stemcr.2018.03.003.

62. Reichwald, J., Danner, S., Wiederhold, K.H., and Staufenbiel, M. (2009). Expression of complement system components during aging and amyloid deposition in APP transgenic mice. J. Neuroinflammation *6*, 35. https://doi.org/10.1186/1742-2094-6-35.

63. Shi, Q., Chowdhury, S., Ma, R., Le, K.X., Hong, S., Caldarone, B.J., Stevens, B., and Lemere, C.A. (2017). Complement C3 deficiency protects against neurodegeneration in aged plaque-rich APP/PS1 mice. Sci. Transl. Med. *9*, eaaf6295. https://doi.org/10.1126/scitranslmed.aaf6295.

64. Dejanovic, B., Huntley, M.A., De Mazière, A., Meilandt, W.J., Wu, T., Srinivasan, K., Jiang, Z., Gandham, V., Friedman, B.A., Ngu, H., et al. (2018). Changes in the Synaptic Proteome in Tauopathy and Rescue of Tau-Induced Synapse Loss by C1q Antibodies. Neuron *100*, 1322–1336.e7. https://doi.org/10.1016/j.neuron.2018.10.014.

65. Wu, T., Dejanovic, B., Gandham, V.D., Gogineni, A., Edmonds, R., Schauer, S., Srinivasan, K., Huntley, M.A., Wang, Y., Wang, T.M., et al. (2019). Complement C3 Is Activated in Human AD Brain and Is Required for Neurodegeneration in Mouse Models of Amyloidosis and Tauopathy. Cell Rep. *28*, 2111–2123.e6. https://doi.org/10.1016/j.celrep.2019.07.060.

66. Allen, G., Barnard, H., McColl, R., Hester, A.L., Fields, J.A., Weiner, M.F., Ringe, W.K., Lipton, A.M., Brooker, M., McDonald, E., et al. (2007).

Reduced hippocampal functional connectivity in Alzheimer disease. Arch. Neurol. *64*, 1482–1487. https://doi.org/10.1001/archneur.64.10.1482.

67. Trujillo-Estrada, L., Dávila, J.C., Sánchez-Mejias, E., Sánchez-Varo, R., Gomez-Arboledas, A., Vizuete, M., Vitorica, J., and Gutiérrez, A. (2014). Early neuronal loss and axonal/presynaptic damage is associated with accelerated amyloid-beta accumulation in AbetaPP/PS1 Alzheimer's disease mice subiculum. J. Alzheimers Dis. *42*, 521–541. https://doi.org/10.3233/JAD-140495.

68. Brown, G.D., Willment, J.A., and Whitehead, L. (2018). C-type lectins in immunity and homeostasis. Nat. Rev. Immunol. *18*, 374–389. https://doi.org/10.1038/s41577-018-0004-8.

69. Linnartz, B., and Neumann, H. (2013). Microglial activatory (immunoreceptor tyrosine-based activation motif)- and inhibitory (immunoreceptor tyrosine-based inhibition motif)-signaling receptors for recognition of the neuronal glycocalyx. Glia *61*, 37–46. https://doi.org/10.1002/glia.22359.

70. Toker, A., and Cantley, L.C. (1997). Signalling through the lipid products of phosphoinositide-3-OH kinase. Nature *387*, 673–676. https://doi.org/10.1038/42648.

71. Lin, P.B.C., Tsai, A.P.Y., Soni, D., Lee-Gosselin, A., Moutinho, M., Puntambekar, S.S., Landreth, G.E., Lamb, B.T., and Oblak, A.L. (2023). INPP5D deficiency attenuates amyloid pathology in a mouse model of Alzheimer's disease. Alzheimers Dement. *19*, 2528–2537. https://doi.org/10.1002/alz.12849.

72. Deczkowska, A., Keren-Shaul, H., Weiner, A., Colonna, M., Schwartz, M., and Amit, I. (2018). Disease-Associated Microglia: A Universal Immune Sensor of Neurodegeneration. Cell *173*, 1073–1081. https://doi.org/10.1016/j.cell.2018.05.003.

73. Scott-Hewitt, N., Perrucci, F., Morini, R., Erreni, M., Mahoney, M., Witkowska, A., Carey, A., Faggiani, E., Schuetz, L.T., Mason, S., et al. (2020). Local externalization of phosphatidylserine mediates developmental synaptic pruning by microglia. EMBO J. *39*, e105380. https://doi.org/10.15252/embj.2020105380.

74. Tagliatti, E., Desiato, G., Mancinelli, S., Bizzotto, M., Gagliani, M.C., Faggiani, E., Hernández-Soto, R., Cugurra, A., Poliseno, P., Miotto, M., et al. (2024). Trem2 expression in microglia is required to maintain normal neuronal bioenergetics during development. Immunity *57*, 86–105.e9. https://doi.org/10.1016/j.immuni.2023.12.002.

75. Carpanini, S.M., Torvell, M., Bevan, R.J., Byrne, R.A.J., Daskoulidou, N., Saito, T., Saido, T.C., Taylor, P.R., Hughes, T.R., Zelek, W.M., and Morgan, B.P. (2022). Terminal complement pathway activation drives synaptic loss in Alzheimer's disease models. Acta Neuropathol. Commun. *10*, 99. https://doi.org/10.1186/s40478-022-01404-w.

76. Stevens, B., and Johnson, M.B. (2021). The complement cascade repurposed in the brain. Nat. Rev. Immunol. *21*, 624–625. https://doi.org/10.1038/s41577-021-00621-z.

77. Heath, L., Earls, J.C., Magis, A.T., Kornilov, S.A., Lovejoy, J.C., Funk, C.C., Rappaport, N., Logsdon, B.A., Mangravite, L.M., Kunkle, B.W., et al. (2022). Manifestations of Alzheimer's disease genetic risk in the blood are evident in a multiomic analysis in healthy adults aged 18 to 90. Sci. Rep. *12*, 6117. https://doi.org/10.1038/s41598-022-09825-2.

78. Chou, V., Fancher, S.B., Pearse, R.V., Lee, H., Lam, M., Seyfried, N.T., Bennett, D.A., De Jager, P.L., Menon, V., and Young-Pearse, T.L. (2023). INPP5D/SHIP1 regulates inflammasome activation in human microglia. Preprint at bioRxiv. https://doi.org/10.1101/2023.02.25.530025.

79. Fernandes, S., Srivastava, N., Sudan, R., Middleton, F.A., Shergill, A.K., Ryan, J.C., and Kerr, W.G. (2018). SHIP1 Deficiency in Inflammatory Bowel Disease Is Associated With Severe Crohn's Disease and Peripheral T Cell Reduction. Front. Immunol. *9*, 1100. https://doi.org/10.3389/fimmu.2018.01100.

80. Ledo, J.H., Azevedo, E.P., Medrihan, L., Cheng, L., Silva, H.M., McCabe, K., Bamkole, M., Lafaille, J.J., Friedman, J.M., Stevens, B., and G., P. (2021). A Developmental Role for Microglial Presenilin 1 in Memory. Preprint at bioRXiv.

81. Burgess, N., Maguire, E.A., and O'Keefe, J. (2002). The human hippocampus and spatial and episodic memory. Neuron *35*, 625–641. https://doi.org/10.1016/s0896-6273(02)00830-9.

82. Haettig, J., Sun, Y., Wood, M.A., and Xu, X. (2013). Cell-type specific inactivation of hippocampal CA1 disrupts location-dependent object recognition in the mouse. Learn. Mem. *20*, 139–146. https://doi.org/10.1101/lm.027847.112.

83. Broadbent, N.J., Squire, L.R., and Clark, R.E. (2004). Spatial memory, recognition memory, and the hippocampus. Proc. Natl. Acad. Sci. USA *101*, 14515–14520. https://doi.org/10.1073/pnas.0406344101.

84. Cekic, C., Casella, C.R., Sag, D., Antignano, F., Kolb, J., Suttles, J., Hughes, M.R., Krystal, G., and Mitchell, T.C. (2011). MyD88-dependent SHIP1 regulates proinflammatory signaling pathways in dendritic cells after monophosphoryl lipid A stimulation of TLR4. J. Immunol. *186*, 3858–3865. https://doi.org/10.4049/jimmunol.1001034.

85. Ganesan, L.P., Joshi, T., Fang, H., Kutala, V.K., Roda, J., Trotta, R., Lehman, A., Kuppusamy, P., Byrd, J.C., Carson, W.E., et al. (2006). FcgammaR-induced production of superoxide and inflammatory cytokines is differentially regulated by SHIP through its influence on PI3K and/or Ras/Erk pathways. Blood *108*, 718–725. https://doi.org/10.1182/blood-2005-09-3889.

86. An, H., Xu, H., Zhang, M., Zhou, J., Feng, T., Qian, C., Qi, R., and Cao, X. (2005). Src homology 2 domain-containing inositol-5-phosphatase 1 (SHIP1) negatively regulates TLR4-mediated LPS response primarily through a phosphatase activity- and PI-3K-independent mechanism. Blood *105*, 4685–4692. https://doi.org/10.1182/blood-2005-01-0191.

87. Terzioglu, G., and Young-Pearse, T.L. (2023). Microglial function, INPP5D/SHIP1 signaling, and NLRP3 inflammasome activation: implications for Alzheimer's disease. Mol. Neurodegener. *18*, 89. https://doi.org/10.1186/s13024-023-00674-9.

88. Schneider, C.A., Rasband, W.S., and Eliceiri, K.W. (2012). NIH Image to ImageJ: 25 years of image analysis. Nat. Methods *9*, 671–675. https://doi.org/10.1038/nmeth.2089.

89. Dobin, A., Davis, C.A., Schlesinger, F., Drenkow, J., Zaleski, C., Jha, S., Batut, P., Chaisson, M., and Gingeras, T.R. (2013). STAR: ultrafast universal RNA-seq aligner. Bioinformatics *29*, 15–21. https://doi.org/10.1093/bioinformatics/bts635.

90. Liao, Y., Smyth, G.K., and Shi, W. (2014). featureCounts: an efficient general purpose program for assigning sequence reads to genomic features. Bioinformatics *30*, 923–930. https://doi.org/10.1093/bioinformatics/btt656.

91. Love, M.I., Huber, W., and Anders, S. (2014). Moderated estimation of fold change and dispersion for RNA-seq data with DESeq2. Genome Biol. *15*, 550. https://doi.org/10.1186/s13059-014-0550-8.

92. Young, M.D., and Behjati, S. (2020). SoupX removes ambient RNA contamination from droplet-based single-cell RNA sequencing data. GigaScience *9*, giaa151. https://doi.org/10.1093/gigascience/giaa151.

93. Wolock, S.L., Lopez, R., and Klein, A.M. (2019). Scrublet: Computational Identification of Cell Doublets in Single-Cell Transcriptomic Data. Cell Syst. *8*, 281–291.e9. https://doi.org/10.1016/j.cels.2018.11.005.

94. Hao, Y., Hao, S., Andersen-Nissen, E., Mauck, W.M., 3rd, Zheng, S., Butler, A., Lee, M.J., Wilk, A.J., Darby, C., Zager, M., et al. (2021). Integrated analysis of multimodal single-cell data. Cell *184*, 3573–3587.e29. https://doi.org/10.1016/j.cell.2021.04.048.

95. Korsunsky, I., Millard, N., Fan, J., Slowikowski, K., Zhang, F., Wei, K., Baglaenko, Y., Brenner, M., Loh, P.R., and Raychaudhuri, S. (2019). Fast, sensitive and accurate integration of single-cell data with Harmony. Nat. Methods *16*, 1289–1296. https://doi.org/10.1038/s41592-019-0619-0.

96. Bray, N.L., Pimentel, H., Melsted, P., and Pachter, L. (2016). Near-optimal probabilistic RNA-seq quantification. Nat. Biotechnol. *34*, 525–527. https://doi.org/10.1038/nbt.3519.

97. Kreitzer, F.R., Salomonis, N., Sheehan, A., Huang, M., Park, J.S., Spindler, M.J., Lizarraga, P., Weiss, W.A., So, P.L., and Conklin, B.R.

Immunity
Article

(2013). A robust method to derive functional neural crest cells from human pluripotent stem cells. Am. J. Stem Cells 2, 119–131.

98. Mattei, D., Ivanov, A., van Oostrum, M., Pantelyushin, S., Richetto, J., Mueller, F., Beffinger, M., Schellhammer, L., Vom Berg, J., Wollscheid, B., et al. (2020). Enzymatic Dissociation Induces Transcriptional and Proteotype Bias in Brain Cell Populations. Int. J. Mol. Sci. 21, 7944. https://doi.org/10.3390/ijms21217944.

99. Puvogel, S., Alsema, A., North, H.F., Webster, M.J., Weickert, C.S., and Eggen, B.J.L. (2024). Single-Nucleus RNA-Seq Characterizes the Cell Types Along the Neuronal Lineage in the Adult Human Subependymal Zone and Reveals Reduced Oligodendrocyte Progenitor Abundance with Age. eNeuro 11, ENEURO.0246-23.2024. https://doi.org/10.1523/ENEURO.0246-23.2024.

100. Pietilä, R., Del Gaudio, F., He, L., Vázquez-Liébanas, E., Vanlandewijck, M., Muhl, L., Mocci, G., Bjørnholm, K.D., Lindblad, C., Fletcher-Sandersjöö, A., et al. (2023). Molecular anatomy of adult mouse leptomeninges. Neuron 111, 3745–3764.e7. https://doi.org/10.1016/j.neuron.2023.09.002.

101. Vanlandewijck, M., He, L., Mäe, M.A., Andrae, J., Ando, K., Del Gaudio, F., Nahar, K., Lebouvier, T., Laviña, B., Gouveia, L., et al. (2018). A molecular atlas of cell types and zonation in the brain vasculature. Nature 554, 475–480. https://doi.org/10.1038/nature25739.

102. Hodge, R.D., Bakken, T.E., Miller, J.A., Smith, K.A., Barkan, E.R., Graybuck, L.T., Close, J.L., Long, B., Johansen, N., Penn, O., et al. (2019). Conserved cell types with divergent features in human versus mouse cortex. Nature 573, 61–68. https://doi.org/10.1038/s41586-019-1506-7.

103. Wei, J.R., Hao, Z.Z., Xu, C., Huang, M., Tang, L., Xu, N., Liu, R., Shen, Y., Teichmann, S.A., Miao, Z., and Liu, S. (2022). Identification of visual cortex cell types and species differences using single-cell RNA sequencing. Nat. Commun. 13, 6902. https://doi.org/10.1038/s41467-022-34590-1.

104. Pelkey, K.A., Chittajallu, R., Craig, M.T., Tricoire, L., Wester, J.C., and McBain, C.J. (2017). Hippocampal GABAergic Inhibitory Interneurons. Physiol. Rev. 97, 1619–1747. https://doi.org/10.1152/physrev.00007.2017.

105. Bezaire, M.J., and Soltesz, I. (2013). Quantitative assessment of CA1 local circuits: knowledge base for interneuron-pyramidal cell connectivity. Hippocampus 23, 751–785. https://doi.org/10.1002/hipo.22141.

106. Frazer, S., Prados, J., Niquille, M., Cadilhac, C., Markopoulos, F., Gomez, L., Tomasello, U., Telley, L., Holtmaat, A., Jabaudon, D., and Dayer, A. (2017). Transcriptomic and anatomic parcellation of 5-HT(3A)R expressing cortical interneuron subtypes revealed by single-cell RNA sequencing. Nat. Commun. 8, 14219. https://doi.org/10.1038/ncomms14219.

107. Lim, L., Mi, D., Llorca, A., and Marín, O. (2018). Development and Functional Diversification of Cortical Interneurons. Neuron 100, 294–313. https://doi.org/10.1016/j.neuron.2018.10.009.

108. Bowles, K.R., Tcw, J., Qian, L., Jadow, B.M., and Goate, A.M. (2019). Reduced variability of neural progenitor cells and improved purity of neuronal cultures using magnetic activated cell sorting. PLoS One 14, e0213374. https://doi.org/10.1371/journal.pone.0213374.

109. Leggio, L., L'Episcopo, F., Magrì, A., Ulloa-Navas, M.J., Paternò, G., Vivarelli, S., Bastos, C.A.P., Tirolo, C., Testa, N., Caniglia, S., et al. (2022). Small Extracellular Vesicles Secreted by Nigrostriatal Astrocytes Rescue Cell Death and Preserve Mitochondrial Function in Parkinson's Disease. Adv. Healthc. Mater. 11, e2201203. https://doi.org/10.1002/adhm.202201203.

CellPress
OPEN ACCESS

Immunity
Article

STAR★METHODS

KEY RESOURCES TABLE

REAGENT or RESOURCE	SOURCE	IDENTIFIER
Antibodies		
Monoclonal mouse anti-PSD95 (clone 6G6-1C9)	Millipore	Cat# MAB1596; RRID: AB_2092365
Monoclonal mouse anti-GAPDH	Proteintech	Cat# 60004-1-Ig; RRID: AB_2107436
Monoclonal mouse anti-VGAT (cytoplasmic domain)	Synaptic Systems	Cat# 131011; RRID: AB_2619818
Monoclonal mouse anti-GEPHYRIN	Synaptic Systems	Cat# 147111;RRID: AB_887719
Polyclonal rabbit anti-SHIP1 (D1163)	Cell Signaling Technology	Cat# 2728;RRID: AB_2126244
Monoclonal mouse anti-SHIP1 (P1C1)	Santa Cruz Biotechnology	Cat# sc-8425;RRID: AB_628250
Monoclonal mouse anti-β-ACTIN	Proteintech	Cat# 60008-1-Ig; RRID: AB_2289225
Monoclonal mouse anti-β-ACTIN	Sigma-Aldrich	Cat# A1978; RRID: AB_476692
Polyclonal rabbit anti-IBA1	FUJIFILM Wako Pure Chemical Corporation	Cat# 019-19741; RRID: AB_839504
Monoclonal mouse anti-IBA1	Merck Millipore	Cat# MAbN92; RRID: AB_10917271
Monoclonal mouse anti-IBA1 (clone 20A12.1)	Sigma Aldrich	Cat# ZMS1024
Monoclonal mouse anti-GFAP	Sigma-Aldrich	Cat# G3893; RRID: AB_477010
Monoclonal rabbit anti-GAPDH	Abcam	Cat# ab181602; RRID: AB_2630358
Monoclonal rat anti-CD68	Bio-Rad	Cat# MCA1957; RRID: AB_322219
Polyclonal guinea pig anti-PSD-95	Synaptic Systems	Cat# 124014;RRID: AB_2619800
Polyclonal guinea pig anti-vGLUT1	Synaptic Systems	Cat# 135304;RRID: AB_887878
Monoclonal rabbit anti-C1Q	Abcam	Cat# ab182451; RRID: AB_2732849
Polyclonal rabbit anti-GFAP	Dako	Cat# Z0334;RRID: AB_10013382
Polyclonal rabbit anti-OLIG2	Sigma-Aldrich	Cat# AB9610;RRID: AB_570666
Polyclonal goat anti-SOX2	Biotechne	Cat# AF2018;RRID: AB_355110
Chicken anti-GFP	AvesLab	Cat# 1010
Monoclonal mouse anti-NEUN (clone A60, AF488)	Merck	Cat# MAB377X
Polyclonal rabbit anti-OLIG2 (AF647)	Novus Biologicals	Cat# NBP2-41269
Monoclonal mouse anti-CD63	MBL Life Science	Cat# D263-3; RRID:AB_1278815
Monoclonal rat anti-CD9	BD Pharmigen	Cat# 553758; RRID: AB_395032
Polyclonal rabbit anti-CALNEXIN	Abcam	Cat# ab22595; RRID: AB_2069006
Monoclonal rat anti-Dectin1 (CLEC7A, clone R1-8g7)	Invivogen	Cat# magb-mdect-2
Polyclonal rabbit anti-NEUN	Invitrogen	Cat# PA5-78499; RRID: AB_2736206
IRDye 800CW Donkey anti-Mouse IgG	LI-COR	Cat# 926-32212; RRID: AB_621847
IRDye 800CW Donkey anti-Rabbit IgG	LI-COR	Cat# 926-32213; RRID: AB_621848
IRDye 680RD Donkey anti-Mouse IgG	LI-COR	Cat# 926-68072; RRID: AB_10953628
IRDye® 680RD Donkey Anti-Rabbit IgG	LI-COR	Cat# 926-68073; RRID: AB_10954442
IRDye® 680RD Donkey Anti-Guinea Pig IgG	LI-COR	Cat# 926-68077; RRID: AB_10956079
Alexa Fluor Plus 647, Donkey anti-Rabbit IgG (H+L)	Thermo Fisher Scientific	Cat# A32795; RRID: AB_2762835
Alexa Fluor Plus 555, Donkey anti-Mouse IgG (H+L)	Thermo Fisher Scientific	Cat# A32773; RRID: AB_2762848
Alexa Fluor Plus 488, Donkey anti-Rabbit IgG (H+L)	Thermo Fisher Scientific	Cat# A21206; RRID: AB_2535792
Alexa Fluor Plus 488, Donkey anti-Goat IgG (H+L)	Thermo Fisher Scientific	Cat# A32814; RRID: AB_2762838
Alexa Fluor Plus 555, Donkey anti-Rat IgG (H+L)	Thermo Fisher Scientific	Cat# A48270; RRID: AB_2896336
Alexa Fluor Plus 555, Donkey anti-Rabbit IgG (H+L)	Thermo Fisher Scientific	Cat# A-31572; RRID: AB_162543
Alexa Fluor Plus 555, Goat anti-Guinea Pig IgG (H+L)	Thermo Fisher Scientific	Cat# A-21435; RRID: AB_2535856
Alexa Fluor Plus 647, Donkey anti-Mouse IgG (H+L)	Thermo Fisher Scientific	Cat# A32787; RRID: AB_2762830
Goat anti-Mouse IgG2b Cross-Adsorbed Secondary Antibody, Alexa Fluor™ 488	Thermo Fisher Scientific	Cat# A-21141; RRID: AB_141626

Continued

REAGENT or RESOURCE	SOURCE	IDENTIFIER
Fluoresceinated Goat Anti-Chicken IgY Secondary Antibody	AvesLab	Cat# F-1005; RRID: AB_2313516
Goat Anti-Rabbit IgG Antibody (H+L), Peroxidase	Vector Laboratories	Cat# PI-1000; RRID: AB_2916034
Horse Anti-Mouse IgG Antibody (H+L), Peroxidase	Vector Laboratories	Cat# PI-2000; RRID: AB_2336177
HRP-conjugated anti-Rat	Invitrogen	Cat# 31470; RRID: AB_228356
HRP-conjugated anti-Rabbit	Invitrogen	Cat# 31460; RRID: AB_228341
HRP-conjugated anti-Mouse	Dako	Cat# P044
HRP-conjugated anti-Mouse	Cell Signaling Technology	Cat# 7076; RRID: AB_330924
Bacterial and virus strains		
AAV-mScarlet	This paper	N/A
AAV-CD55-p2A-mScarlet	This paper	N/A
Chemicals, peptides, and recombinant proteins		
Tamoxifen	Sigma-Aldrich	Cat# T5648
Paraformaldehyd	Sigma-Aldrich	Cat# 16005
Sodium Azide	Roth	Cat# K305.1
Poly-D-Lysin-hydrobromid	Sigma-Aldrich	Cat# P7886
Cre Recombinase, TAT-Cre (Tat-NLS-Cre, HTNC, HTNCre)	Labgene	Cat# EG-1001
Beta-Amyloid (1-40), HiLyte™ Fluor 488-labeled	Eurogentec	Cat# AS-60491-01
Dimethyl sulphoxide (DMSO)	Roth	Cat# A994.1
pHrodo iFL Green STP ester	Life Technologies	Cat# P36012
pHrodo™ Red, succinimidyl ester	Thermo Fisher Scientific	Cat# P36600
CytochalasinD	Sigma-Aldrich	Cat# C8273
Bafilomycin	Hello Bio	Cat# HB1125
Triton X-100	Sigma-Merck	Cat# X100
Bovine serum albumin (BSA)	VWR	Cat# 9048-46-8
DAPI	Thermo Fisher Scientific	Cat# D1306
Mowiol 4-88	Sigma-Aldrich	Cat# 81381
Thioflavin-S	Sigma-Aldrich	Cat# T1892
TRI Reagent	Thermo Fisher Scientific	Cat# AM9738
Alt-R™ S.p. Cas9 Nuclease V3	IDT	Cat# 1081058
Insulin solution Human	Sigma-Aldrich	Cat# I9278
Recombinant Human IL-34	PeproTech	Cat# 200-34
Recombinant Human TGF-β1	PeproTech	Cat# 100-21
Recombinant Human M-CSF	PeproTech	Cat# 300-31
Recombinant Human Fractalkine (CX3CL1)	PeproTech	Cat# 300-25
Recombinant Human CD200 (C-His)	Bon Opus Biosciences	Cat# BP004
Tris Base	Fisher Scientific	Cat# BP152
Sodium Chloride	Sigma Aldrich	Cat# S7653
Sodium deoxycholate	Sigma Aldrich	Cat# 30970
Sodium dodecyl sulfate	Sigma Aldrich	Cat# 71736
EDTA 0,5 M, sterile solution	VWR chemicals	Cat# E177-100ML
Phenylmethanesulfonyl fluoride solution (PMSF)	Sigma Aldrich	Cat# 93482
BSA	Pierce	Cat# 23210
Chroman 1	MedChem Express	Cat# HY-15392
Critical commercial assays		
KAPA Mouse Genotyping Kit	Sigma-Aldrich	Cat# KK7302
MACS Neural Tissue Dissociation Kit (P)	Miltenyi biotech	Cat#130-092-628
Syn-PER™ Synaptic Protein Extraction Reagent	Thermo Fisher Scientific	Cat# 87793
Pierce™ BCA Protein Assay Kit	Thermo Fisher Scientific	Cat# 23227
WesternBright ECL	Advansta	Cat# K-12045-D20

Continued

REAGENT or RESOURCE	SOURCE	IDENTIFIER
Supersignal West PICO	Thermo Fisher Scientific	Cat# 34577
WesternBright Sirius	Advansta	Cat# K-12043-C20
Mouse C1qa (Complement C1q subcomponent subunit A) ELISA Kit	#FineTest	Cat# EM0450
Mouse INPP5D / SHIP1 / SHIP (Competitive EIA) ELISA Kit	#LS Bio	Cat# LS-F20238-1
DNAse I Kit	ThermoFisher Scientific	Cat# EN0521
iScript cDNA Synthesis Kit	Bio-Rad	Cat# 170-8891
SensiFAST SYBR Lo-ROX Kit	Bioline	Cat# BIO94020
QuickExtract DNA extraction solution	Lucigen	Cat# QE090500
DreamTaq DNA Polymerase	Thermo Fisher Scientific	Cat# EP0702
STEMdiff™ Hematopoietic Kit	StemCell Technologies	Cat# 05310
Chromium Next GEM Single Cell 3' GEM, Library & Gel Bead Kit v3.1, 16 rxns	10x Genomics	Cat# PN-1000121
Dual Index Kit TT Set A, 96 rxns	10x Genomics	Cat# PN-1000215
SPLIT RNA Extraction Kit	Lexogen	Cat# K00848
P3 Primary Cell 4D-Nucleofector® X Kit L	Lonza	Cat# V4XP-3024
Percoll PLUS density gradient media	Cytiva	Cat# 17544502
CD11b MicroBeads, human and mouse	Miltenyi biotec	Cat# 130-097-142
LS Columns	Miltenyi biotec	Cat# 130-042-401
DC Protein Assay	Biorad	Cat# 500-0116
Deposited data		
Bulk RNA-seq of hippocampal mouse microglia	GEO repository	GSE268277
Single nuclei RNA sequencing from mouse hippocampi	GEO repository	GSE264452
Proteomic from mouse hippocampi	ProteomeXchange Consortium	PXD052118
Bulk RNA-sequencing of human IPSCs-derived microglia	GEO repository	GSE279176
Experimental models: Cell lines		
BV-2 microglia cell line (Parental)		RRID: CVCL_0182
BV-2 microglia cell line (SHIP1 KO single clone)	Generated by Pedicone, Fernandes, Matera et al.[36]	PMID: 35465359
IPSC WTC11		RRID:CVCL_Y803
Experimental models: Organisms/strains		
C57Bl/6J	The Jackson Laboratory	Cat# 000664
B6.129S6-Inpp5dtm1Wgk/J	The Jackson Laboratory	Cat# 028255
B6.129P2(Cg) Cx3cr1tm2.1(cre/ERT2)Litt/WganJ	The Jackson Laboratory	Cat# 021160
B6.Cg-Tg(Camk2a-cre)T29-1Stl/J	The Jackson Laboratory	Cat# 005359
Gt(ROSA)26Sortm14(CAG-tdTomato)Hze	The Jackson Laboratory	Cat# 007914
ArcAbeta (tghAPPswe,arc)	Kind gift from Prof. Roger Nitsch	N/A
Oligonucleotides		
Inpp5d Forward ACTGATTTCCCAAGTGCTTCT (Genotype)	Microsynth	N/A
Inpp5d Reverse CCTTGAACACCTCTGCCAAC (Genotype)	Microsynth	N/A
Ppia FW: CAAATGCTGGACCAAACACAA	Microsynth	N/A
Ppia RV: GTTCATGCCTTCTTTCACCTTC	Microsynth	N/A
Rplp0 FW: TCGTTGGAGTGACATCGTCTT	Microsynth	N/A
Rplp0 RV: GATCTGCTGCATCTGCTTGG	Microsynth	N/A
B2m FW: CTCGGTGACCCTGGTCTTTC	Microsynth	N/A
B2m RV: TTGAGGGGTTTTCTGGATAGC	Microsynth	N/A
Inpp5d FW: CTGTTCAGGCATCCGAAGGT (qRT-PCR)	Microsynth	N/A
Inpp5d RV: AGTGTCCTCCTCAGCCTCAT (qRT-PCR)	Microsynth	N/A

Continued

REAGENT or RESOURCE	SOURCE	IDENTIFIER
Software and algorithms		
ImageJ	Schneider et al.[88]	RRID: SCR_003070
Imaris	Oxford Instruments	RRID: SCR_007370
ViiA 7 Real-Time PCR System	Applied Biosystems	RRID: SCR_023358
Mini Analysis software	Synaptosoft	RRID: SCR_002184
Sartorius Live-Cell Imaging	Sartorius	RRID: SCR_023147
Biorender	Biorender	RRID: SCR_018361
EthoVision XT	Noldus	RRID: SCR_000441
Graphpad Prism, version 9.3.1	GraphPad Software	RRID: SCR_000306
ChemiDoc XRS+ imaging system	Bio-Rad	RRID: SCR_019690
LI-COR Odyssey Fc Imaging System	LI-COR	RRID: SCR_023227
Image studio Lite	LI-COR	RRID: SCR_013715
STAR, version-2.7.3a	Dobin et al.[89]	RRID: SCR_004463
FeatureCounts, version 2.0.0	Liao et al.[90]	RRID: SCR_012919
DESeq2, version 1.32.0	Love et al.[91]	RRID: SCR_015687
CERNO, version 0.50.07	Zyla et al.[27]	N/A
Cell Ranger, version 7	10x Genomics	RRID: SCR_017344
SoupX	Young et al.[92]	RRID: SCR_019193
Scrublet	Wolock et al.[93]	RRID: SCR_018098
Seurat, version 4.3	Hao et al.[94]	RRID: SCR_016341
Harmony	Korsunsky et al.[95]	RRID: SCR_022206
R	R	RRID: SCR_002394
R package MAST, version 1.24.1	https://doi.org/10.5281/zenodo.18539	RRID:SCR_016340
SynGO	Koopmans et al.[41]	RRID:SCR_017330
CellChat	Jin et al.[42]	RRID:SCR_021946
Kallisto	Bray et al.[96]	RRID:SCR_016582
Other		
Vibratome VT1200S	Leica	RRID: SCR_018453
Nanosight NS300 analyzer	Malvern	N/A
BX51WI upright microscope	Olympus	RRID: SCR_023069
Stellaris 5 confocal laser scanning system	Leica	RRID: SCR_024663
Synergy MX	BioTek	N/A
Miltenyi gentleMACS Dissociator	Milteny biotec	Cat# 130-093-235
QuadroMACS™ Separator and Starting Kits	Milteny biotec	Cat# 130-091-051
Pierce Protease and Phosphatase Inhibitor Mini Tablets,EDTA-free	Thermo Fisher Scientific	Cat# A32961
TripLE Express Enzyme Solution	Thermo Fisher Scientific	Cat# 12-604-021
RIPA Lysis Buffer, 10X	Merck	Cat# 20-188
4-15% Mini-PROTEAN TGX Gels	Bio-Rad	Cat# 4561086 or Cat#4561084
Trans-Blot Turbo Midi Nitrocellulose	Bio-Rad	Cat# 170-4159
REVERT Total Protein Stain Solution	Li-Cor	Cat# 926-11011
Heparin coated tubes	Laborimpex	Cat# 41.1393.005
PBS 1X	Thermo Fisher Scientific	Cat# 10010-056
Geltrex™ LDEV-Free, hESC-Qualified, Reduced Growth Factor Basement Membrane Matrix	Thermo Fisher Scientific	Cat# A1413301
mTeSR™ Plus	Stemcell Technologies	Cat# 100-0276
StemFlex™ Medium	Thermo Fisher Scientific	Cat# A3349401
Matrigel	Corning	Cat# 356231
Matrigel® Growth Factor Reduced (GFR)	Corning	Cat# 354230

(Continued on next page)

Continued

REAGENT or RESOURCE	SOURCE	IDENTIFIER
DMEM/F-12, HEPES	Gibco	Cat# 11330032
Insulin-Transferrin-Selenium (ITS -G)	Thermo Scientific	Cat# 41400045
1-Thioglycerol	Sigma-Aldrich	Cat# M1753
Lysis buffer M-PER™	Thermo Fisher Scientific	Cat# 78501
Halt™ Protease and Phosphatase Inhibitor Cocktail, EDTA-free (100X)	Thermo Fisher Scientific	Cat# PI78441
Halt™ Phosphatase inhibitor cocktail	Thermo Fisher Scientific	Cat# 78420
4-12% Bis Tris Plus Gel for reducing SDS page	Invitrogen	Cat# NW04125BOX, NP0007, B0009
20X Bolt™ MES SDS Running Buffer	Invitrogen	Cat# B0002
MEM Non-Essential Amino Acids Solution (NEAA)	Thermo Fisher Scientific	Cat# 11140050
N-2 Supplement (100X)	Thermo Fisher Scientific	Cat# 17502048
B-27™ Supplement (50X), serum free	Thermo Fisher Scientific	Cat# 17504044
DMEM, high glucose, pyruvate	Thermo Fisher Scientific	Cat# 11995073
Glutamax™ Supplement	Thermo Fisher Scientific	Cat# 35050061
Fetal Bovine Serum, exosome-depleted	Thermo Fisher Scientific	Cat# A2720801
Ultra-cone polyclear centrifuge tubes	Seton	Cat# 7067
Thick wall polycarbonate tubes	Seton	Cat# 2002
Complete Protease inhibitor cocktail	Roche	Cat# 04693116001
Accutase Cell Detachment Solution	Innovative Cell Technologies, Inc.	Cat# AT104-500
Fetal Bovine Serum, qualified, heat inactivated, Brazil	Thermo Fisher Scientific	Cat# 10500064
Penicillin-Streptomycin (10,000 U/mL)	Thermo Fisher Scientific	Cat# 15140122

EXPERIMENTAL MODEL AND STUDY PARTICIPANT DETAILS

Animals

All animal experiments were authorized by the 'Service de la consommation et des Affaires vétérinaires' (SCAV) of the Canton de Vaud in Switzerland. Mice were purchased from The Jackson laboratory (C57Bl/6J, B6.129S6-Inpp5dtm1Wgk/J, Strain: #028255. B6.129P2(Cg)[54] Cx3cr1tm2.1(cre/ERT2)Litt/WganJ, Strain: #021160).[25] ArcAbeta mice[22] were a kind gift of Prof. Roger Nitsch, University of Zurich. Mice were bred in the animal facility, with food and water *ad libitum*, at 20-22°C. In order to obtain experimental animals, Inpp5d$^{fl/+}$ mice were crossed with Cx3cr1$^{CreErt2-ires-YFP;CreErt2-ires-YFP}$;Inpp5d$^{fl/+}$. The litters were injected with 40μL of tamoxifen (dissolved in 10% EtOH and 90% Corn Oil, at 2 mg/mL. Sigma-Aldrich, #T5648) at P3 and P4. Toe clipping of pups was performed between P6 and P12, followed by DNA extraction (KAPA Mouse Genotyping Kit, Sigma-Aldrich, #KK7302) and genotyping (Inpp5d Forward: 5'-ACT GAT TTC CCA AGT GCT TCT-3'. Inpp5d Reverse: 5'-CCT TGA ACA CCT CTG CCA AC-3'). For the KO induction in adult mice, 200μL of tamoxifen (dissolved in 10% EtOH and 90% Corn Oil, at 10 mg/mL) were intraperitoneally (i.p.) injected for five consecutive days in 3 months old mice. Experiments were carried out on male and female animals. Experiments in pups were performed at P12 or P15 as indicated; experiments in adults at 3 months or 4 months as specified in the text. Mice were housed in groups on a standard 12-h light/12-h dark cycle, and all experiments were performed during the light cycle.

Cell lines and primary cultures

BV2 cells

were cultured in low glucose DMEM (ThermoFisher Scientific) supplemented with 10% fetal bovine serum and 1% Penicillin Streptomycin, at 37°C and 5% CO2 in a humidified incubator.

Microglia Primary Cultures

brains from Inpp5d$^{+/+}$ (Control) or Inpp5d$^{fl/fl}$ (KO), or from Cx3cr1$^{CreErt2-ires-YFP;+}$;Inpp5d$^{+/+}$ (Control) or Cx3cr1$^{CreErt2-ires-YFP;+}$; Inpp5d$^{fl/fl}$ (SHIP1 KO) mice pups at P3-P5 were collected, and cerebellum, meninges and olfactory bulbs were eliminated. Both the hemispheres were mechanically smashed with forceps and put into 3 mL of TripLE Express Enzyme Solution (Thermo Fisher Scientific, #12-604-021) at 37°C for 20min. The tissue was further dissociated by pipetting with a 1 mL tip. Enzymatic reaction was stopped by adding 10 mL of culture medium (DMEM 4.5 g/L of glucose, 10% FBS and 1% pen-strep. Thermo Fisher Scientific, #11995073, #10500064, #15140122). Cells were pelleted at 400g for 4min at RT and the pellet resuspended in fresh culture medium. Cells obtained from each individual brain were seeded into 75 cm^2. After two weeks in culture, microglia were harvested by smacking the flask and seeded (30000 cells/well of a 96 well-plate) on a coating of Poly-D-Lysine (0.1 mg/mL, 1h at 37°C. Sigma-Aldrich, #P7886). Microglial cells were kept in astrocyte-conditioned medium (ACM) and maintained at 37°C and 5% CO2.

Immunity
Article

CellPress
OPEN ACCESS

TAT-cre mediated KO

After one day from Inpp5d^{+/+} or Inpp5d^{fl/fl} primary microglia seeding, cells were treated with 1.75 μM TAT-cre for 2h (Labgene Scientific, #EG1001). Medium was fully changed and TdTomato-labelled synaptosome and 488-labelled amyloid β assays were performed after 4 days, and the KO validation was assessed.

4-Hydroxytamoxifen-mediated KO

Primary microglia isolated from either Cx3cr1[CreErt2-ires-YFP;+];Inpp5d^{+/+} (Control) or Cx3cr1[CreErt2-ires-YFP;+];Inpp5d^{fl/fl} (SHIP1 KO) mice were seeded, and after 24h were incubated with 200nM 4-OH TAM for 72h. Medium was fully changed and phagocytic assay was performed after 24h.

Generation of human INPP5D knockout iPSC lines

The previously described normal induced pluripotent stem cell (iPSC) line WTC11[97] served as the parental line of all CRISPR/Cas9-edited lines used in this study. The gene editing strategy used to generate *INPP5D* homozygous knockout iPSCs was to the strategy used in the Inpp5d knockout mouse model.[26] Briefly, two single guide RNA (sgRNA) 88rev and 326forw, flanking the coding sequence of exon1 were used in combination with a bridging single-stranded oligodeoxynucleotide (ssODN) to mediate the excision of exon 1. To facilitate the identification of homozygous iPSCs, we barcoded the bridging ssODN by inserting two degenerated nucleotides (HB) in between the homology arms. Briefly, one million iPSCs from the WTC-11 donor line (PMID: 23862100) at passage 37 were electroporated using the 4D-Nucleofector System (Lonza, AAF-1003X, V4XP-3024) with a preassembled complex of 10μg of S.p. Cas9 Nuclease (IDT, 1081058), and 4μg of each sgRNA (Synthego, CRISPRevolution sgRNA EZ Kit) and 100 pmol of ssODN (IDT, Alt-R HDR Donor Oligos). Cells were replated on Geltrex (Thermo Fisher, A1413301)-coated plates and incubated in mTeSR Plus (Stemcell Technologies, 100-0276). After five days, single cells were dissociated with Accutase (Innovative CellTechnologies, AT104) sorted into 96-well plates using a WOLF benchtop microfluidic cellsorter (Nanocellect) in mTeSR Plus and 50nM Chroman 1 (MedChem Express HY-15392). After thirteen days, the genomic DNA was extracted from single clones using QuickExtract solution (Lucigen, QE090500) and HDR was verified by locus specific PCR using DreamTaq DNA Polymerase (Thermo Fisher, EP0702) and primers F1 and R1, followed by Sanger sequencing. Sequences of sgRNAs, single-stranded oligodeoxynucleotides (ssODNs), and PCR primers used for CRISPR/Cas9-mediated HDR can be found in Table S3.

hiPSC differentiation into microglia (iMG)

*h*iPSC-derived microglia were differentiated using previously published protocols.[56,57] Briefly, iPSCs were grown in StemFlex (Thermo Fisher Scientific, #A3349401) and seeded (~45 colonies)/plate on Matrigel (Corning, #356231) coated 6 well-plates. iPSCs were differentiated to hematopoietic precursor cells (HPCs) using the STEMdiff™ Hematopoietic Kit (StemCell Technologies, #05310) using manufacturer recommendation. HPCs were harvested and transferred to DMEM/F12 1:1 medium with 4% B27, 0.5% N2, 1% nonessential amino acids (NEAA), 1 mM L-glutamine, Insulin-Transferrin-Selenium (ITS-G), 400uM monothioglycerol (1-Thioglycerol) and 5 μg/mL insulin, supplemented with 100 ng/mL interleukin (IL)-34, 50 ng/mL TGFβ and 25 ng/mL macrophage colony-stimulating factor (M-CSF) for 22 days with media changes every two days and splitting/replating every week. After 22 days, 100 ng/mL CX3CL1 and 100 ng/mL CD200 were added to the media to induce further maturation of iMGs for 3 days. At day 25 from HPC seeding CX3CL1 (100ng/mL) and CD200 (100ng/mL) were added (5F media) to the microglia media to complete maturation. After day 28 microglia were fully mature and used for characterization and assays. Three independent differentiations have been performed for the assays.

METHOD DETAILS

Animal perfusion and brain slicing

Mice were anesthetized with sodium pentobarbital diluted in saline (150mg/kg, i.p.) and perfused with cold HBSS (3ml/min: 10mL for pups and 20mL for adult mice; Thermo Fisher Scientific, #14175129) and PFA 4% (3ml/min: 20mL for pups and 40mL for adult mice; Sigma-Aldrich, #16005). Brains were also post-fixed in cold PFA 4% overnight and stored at 4°C in 0.02% of NaN₃ (Roth, #K305.1) in PBS 1X. Brain slices (60μm thickness) were obtained using Vibratome VT1200S (Leica). When hippocampal dissection was needed, perfusion was performed only with cold HBSS, and the left hemisphere was used. Hippocampus was immediately frozen in dry ice and stored at -80°C.

Acute isolation of microglia

C57BL/6J pups at P15 were anesthetized and perfused intracardially with ice cold HBSS 1X. Tissue was processed according to MACS Neural Tissue Dissociation Kit (P) (Miltenyi biotech, #130-092-628). Brains were quickly removed from the skull, cerebellum and olfactory bulbs were removed, and the remaining tissue was dissected on ice. Tissue was grossly cut in smaller pieces and added to Miltenyi gentleMACS C Tubes. Samples were placed in Miltenyi gentleMACS Dissociator (Miletny biotec, #130-093-235) and the m_brain_01/02/03protocols were run according to manufacturer's instructions. After completion of the program, the samples were briefly spun according to Miltenyi protocol before being filtered through 70μm cell strainer. Samples were washed with HBSS and spun to pellet cells.

Myelin removal was performed using percoll (Cytiva, 17544502) gradient as described in Mattei et al.[98] Pellets were resuspended supplemented with appropriate volume of anti-CD11b microbeads (Miltenyi biotec, 130-097-142) for microglia isolation. Samples

were resuspended in 1mL and passed through an LS column (Miltenyi Biotec, #130-042-401) attached to a MACS Separator (Miltenyi Biotec, #130-091-051). After wash, the column was removed from the magnetic rack and the cells were flushed out in 5 mL of buffer. Samples were centrifuge at 400g 10min 4°C, further washed with 1ml ice cold PBS1X and resuspend in 50μL of RIPA buffer +protease/phosphatase inhibitors (PPI, Thermo Fisher Scientific, #A32961). Samples were stored in -80°C prior to use.

Phagocytic assays in primary microglia
TdTomato-labelled synaptosome assay
TdTomato-labelled synaptosomes were isolated using Syn-PER™ Synaptic Protein Extraction Reagent (Thermo Fisher Scientific, #87793) from CamKII$^{cre/+}$; Rosa26$^{TdTomatoFlox/+}$ mice. After brain collection (excluding cerebellum) and Dounce homogenization on ice, the solution was centrifuged at 1200 × g for 10 min at 4 °C. An additional centrifugation of the supernatant was performed at 15,000 × g for 20 min at 4 °C. The pellet was dissolved in 5% v/v DMSO (Roth, #A994.1) in Syn-PER™ reagent to a final concentration of 6.4μg synaptosome/μL. Aliquots of 50μL were kept at -80 °C. Primary microglia were incubated with 64μg/mL synaptosomes for 1h. After three PBS washes, cells were fixed with 4% PFA to evaluate the amount of the cargo that was taken up (T0) or incubated with fresh medium for 6 h (T6), prior to fixation, to assess synaptosome degradation.

488-pHRodo-labelled synaptosome assay
TdTomato-labelled synaptosome were isolated as described above. pHrodo iFL Green STP ester (Life Technologies, #P36012) was incubated with synaptosomes on a shaker in 100mM sodium bicarbonate buffer, pH 8.5 for 1 hr at RT protected from light, according to manufacturer's instructions (degree of labeling: 12). pHrodo-conjugated synaptosomes were centrifuged at 4°C at 15000 × g for 20 min and the pellet was resuspended in SynPer reagent + 5% DMSO. The final solution was stored at -80°C. Primary microglia were incubated with 1μg/mL and their phagocytic capacity was assessed by live-imaging confocal acquisition.

Bafilomycin and Cytochalasin D experiments
Cells were pre-treated for 30 min with CytochalasinD at 5μM, (Sigma-Aldrich, #C8273) or Bafilomycin at 100nM (Hello Bio, #HB1125) dissolved in DMSO. Cells were then incubated with synaptosomes conjugated with pHrodo +/- Bafilomycin or +/- CytochalasinD for 2h before confocal acquisition. DMSO was used as a control.

Amyloid-β assay
Primary microglia were incubated with 1μM fluorescently labeled-Amyloid ß 1-40 488 (Eurogentec, #AS-60491-01) for 3h (T0). Cells were fixed as described for the synaptosome assay, where T0 and T6 were analyzed.

Western blot
Hippocampal tissue was isolated from C57BL/6J mice, WT control and SHIP1 cKO mice and was lysed in ice-cold RIPA 1× (Merck, #20-188), supplemented with protease inhibitors. Samples were centrifuged at 12,000 × g for 15 min at 4 °C. The supernatant was collected, and protein concentration was quantified with BCA Protein Assay (ThermoFisher Scientific, #23227), following manufacturer's instructions. Reduced samples were run in pre-casted 4-15% Mini-PROTEAN TGX Gels (Bio-Rad, #4561086 or #4561084) and transferred onto nitrocellulose membranes (BioRad, #170-4159) using a semi-dry transfer protocol. Before blocking, the total amount of protein per lane was assessed by REVERT Total Protein Stain Solution (Li-Cor, #926-11011). Membranes were blocked with 3% BSA in TBST (0.02 M Tris base, 0.15 M NaCl, 0.05% Tween-20 in milliQ water, pH 7.2–7.4) for 1h at RT and primary antibodies (diluted in blocking buffer) incubation was performed overnight at 4 °C (PSD95 1:500, Merck-Millipore, #MAB1596. VGLUT1 1:1000, Synaptic Systems, #135304. GAPDH 1:5000, Proteintech, #60004-1-Ig. VGAT 1:1000, Synaptic Systems, #131011. GEPHYRIN 1:1000, Synaptic Systems, #147111. SHIP1, 1:1000, Santa Cruz Biotechnology, #sc-8425, β-actin 1:2000, Proteintech, #60008-1). Unbounded primary antibody was then washed 3× with TBST for 5 min at RT and the membranes were incubated with secondary antibodies (IRDye, 1:15000 in blocking buffer, Li-Cor). After 3 additional washes with TBST, membranes were imaged with the Li-Cor Odyssey system. For SHIP1, membranes were incubated with mouse anti-HRP antibody (Cell Signaling Technology, Cat# 7076, 1:5000) 2 hours at RT. After 3 washes with TBST, membranes were incubated with ECL- WesternBright Sirius (Advansta, K-12043-C20) for 2 minutes and revealed on ChemiDoc XRS+ imaging system (Bio-Rad).

ELISA immunoassays
C1qa ELISA
For mouse plasma collection, C57BL/6J pups at P15 were deeply anesthetized using pentobarbital. A small cut was performed in the right atrium and blood was collected in a heparin coated tubes (laborimpex, 41.1393.005) and placed on ice. Samples were then centrifuged for 10 min, 4000g at 4°C. Plasma was collected and stored in -80°C prior to use. C1qa in plasma samples was analyzed using the mouse C1qa (Complement C1q subcomponent subunit A) ELISA Kit (FineTest, EM0450), using samples diluted 1:100 and following the manufacturer instructions. Samples were run in technical duplicates and absorbance was measured using a microplate reader (Synergy MX, BioTek) at λ=450nm.

SHIP1 ELISA
SHIP1 in brain samples was measured using the mouse INPP5D / SHIP1 / SHIP (Competitive EIA) ELISA Kit (LS Bio, LS-F20238-1). Briefly, mouse cortices from C57BL/6 mice at 2 weeks and 10 weeks of age were homogenate in PBS containing 1X Protease and phosphatase Cocktail inhibitors (PPIs) (Roche #11836170001). Samples were centrifuged at 12,000 × g for 15 min at 4 °C, and the supernatant was used for protein quantification with BCA Protein Assay (ThermoFisher Scientific, #23227). 245 μg of protein were

load per well in 50μl PBS+PPIs total volume, following manufacturer instructions. Samples were run in technical duplicates and absorbance was measured using a microplate reader (Synergy MX, BioTek) at λ=450nm.

Immunofluorescence staining

Brain slices were permeabilized with 0.5% Triton X-100 (Sigma-Merck, #X100) in PBS for 1.5h at RT and blocking was performed with 2% BSA (VWR, #9048-46-8) in permeabilization buffer (1h at RT). Primary antibodies in blocking buffer (Iba1 1:1000, FUJIFILM Wako, #019-19741. SHIP1 1:200, Santa Cruz Biotechnology, #sc-8425. SHIP1 1:200, Cell Signaling, #2728. CD68 1:400, Bio-rad, #MCA1957. PSD95 1:200, Merck-Millipore, #MAB1596. PSD95 1:1200, Synaptic System, #124014. VGLUT1 1:800, Synaptic System, #135304. C1q 1:1000, Abcam, #ab182451. CLEC7a 1:30, Invivogen, #magb-mdect-2. NeuN 1:500, Invitrogen, #PA5-78499. GFAP 1:1000 DAKO, #Z0334. OLIG2 1:400, Merck Millipore, #AB9610. SOX2 1:400, Biotechne, #AF2018. GFP 1:500, AvesLab, #1010) were incubated 4h at RT or overnight at 4°C. After three washes with PBS, samples were incubated with fluorescently labelled secondary antibodies (Alexa Fluor Plus, Thermo Fisher Scientific, or FITC #F-1005, AvesLab), diluted 1:1000 in blocking buffer, for 2h at RT. After three further PBS washes, nuclei were stained for 20 min at RT with DAPI (1μg/ml in PBS. Thermo Fisher Scientific, #D1306). Mowiol 4-88 (Sigma-Aldrich, #81381) was used as mounting medium and the slides dried overnight before the acquisition.

Thioflavin-S Staining

To stain amyloid β-plaques, brain slices were incubated with 1% Thioflavin-S (Sigma-Aldrich, #T1892) in 50% EtOH for 5 minutes at RT. After two washes with 50% EtOH, and one with water, brain sections were left in PBS for 20 minutes, before starting the immunostaining.

Confocal microscopy and imaging analysis

Confocal microscopy was performed by using Stellaris 5 confocal laser scanning system (Leica Microsystems), using a dry 20x or immersion 63x objective. Images were acquired as z-stack, with z-step size of 0.68μm (20x) or 0.3μm (63x). Scale bars are reported in the figure legends. Confocal acquisitions were processed using ImageJ Software or Imaris Software (Bitplane). Images of VGLUT1 puncta in Figures S4G and S4I were acquired using the LIGHTNING super-resolution mode on a Stellaris 5 confocal microscope (Leica Microsystems).

Microglial morphometric analysis and synapse engulfment

3D reconstruction was performed using Imaris Software (Bitplane), with the built-in Surface module. CD68, PSD95 and IBA1 volumes were quantified by applying 3D surface rendering of confocal stacks in their respective channels, using identical settings (fix thresholds of intensity and voxel) within each experiment. For quantification of PSD95 engulfment by microglia, only PSD95 puncta present within microglial CD68+ structures were considered. This procedure was used to ensure that only puncta entirely phagocytosed by microglia were included in the analysis. To this aim, a new channel for "engulfed PSD95" was created, by using the mask function in Imaris, masking the PSD95 signal within CD68+ structures, as previously described.[51]

Filament tracer: Imaris Filament-tracing plugin was used. Starting points were identified setting the largest diameter of soma at 13 μm with smallest value for dendrite diameter at 0.6 μm. Disconnected segments were removed. Fixed thresholds between conditions were applied. Iba1 surfaces, previously reconstructed, were used to analyze number of branches, average and total filament length per cell.

Sholl analysis

Microglia morphology analysis on the cerebellum was conducted using Sholl analysis in ImageJ software with CellShaper, a pack of macros freely available (https://www.achucarro.org/es/downloads/). Briefly, after manual selection of the cell center soma and threshold, the macro automatically generates concentric circles at fixed distances from the soma, obtaining the number of intersections and length of the processes per cell.

Synaptosome and Aβ engulfment assay in primary microglia

Confocal z-stack acquisitions were processed by using ImageJ/FIJI Software: images were max-projected (max intensity) and cell profile was drawn on brightfield signal, and saved as a ROI. Fixed thresholds for signal intensity were applied across experiments, and area covered per cell was measured within each ROI. Efficiency of degradation (delta of the signal) was calculated subtracting the (residual) mean area covered by cargo at T6 from the (initial) mean area covered by cargo at T0. When the acquisition was performed with live-imaging, confocal z-stack acquisitions were taken every 15 minutes for the first hour (uptake), and every hour after the three washes with PBS1X (degradation time point was analyses after 6h from the washes).

Microglial density and CLEC7A-positive microglial density analysis

Microglial density was calculated based on co-localization of IBA1 and DAPI signals. DAPI and IBA1 signals were thresholded using fixed settings within the same experiment. DAPI signal was multiplied by IBA1 signal per each focal plane of the z-stack acquisition, using the "image calculator" function. The resulting mask was max-projected and the identified microglia nuclei were counted with the "analyze particle" function. To measure the percentage of IBA1$^+$CLEC7a$^+$ cells, the method described above was used, substituting the DAPI with the thresholded CLEC7a signal.

C1q quantification of volume within microglia

microglia volumes from confocal z-stack acquisitions were reconstructed using Imaris Software. Per each acquisition, the C1q channel was masked within the microglia volume, to create a channel of "C1q within microglia". Surface rendering was performed on this new channel, and volume quantified and calculated as a percentage of the initial microglia volume.

Quantification of C1q puncta

spot reconstruction and quantification were performed on confocal acquisition using the Spot creation module in Imaris. C1q-positive spots with expected 0.5μm diameter were reconstructed and their number was automatically counted across conditions.

vGLUT1 and PSD95 quantification

vGLUT1 and PSD95 spot reconstruction and quantification was performed on confocal acquisition using the Spot creation module in Imaris. vGLUT1/PSD95-positive spots with expected 0.3μm diameter were reconstructed and their number was automatically counted across conditions. For the synaptic colocalization analysis, only the spots at a distance <0.5μm were considered colocalized.

RNA extraction, retrotranscription and RT-qPCR

Frozen tissues were dissociated passing them into 1mL syringes with different needles (21G, 25G, 27G) in 1mL of TRI Reagent (Thermo- Fisher Scientific, #AM9738). RNA was extracted following manufacturer's instructions and was resuspended in UltraPure DNAse-RNAse-free water. DNAse treatment was performed (DNAse I Kit, ThermoFisher Scientific, #EN0521). 1 μg of RNA was retrotranscribed using the iScript cDNA Synthesis Kit (Bio-Rad, #170-8891), and diluted to 10 ng/μL. Amplicons levels were assessed by SYBR Green dye-emitted fluorescence (SensiFAST SYBR Lo-ROX Kit, Bioline, #BIO94020) using ViiA 7 Real-Time PCR System (ThermoFisher Scientific). Primers sequences are: Ppia FW: CAAATGCTGGACCAAACACAA; Ppia RV: GTTCATGCCTTCTTTCACCTTC; Rplp0 FW: TCGTTGGAGTGACATCGTCTT; Rplp0 RV: GATCTGCTGCATCTGCTTGG; B2m FW: CTCGGTGACCCTGGTCTTTC; B2m RV: TTGAGGGGTTTTCTGGATAGC; Inpp5d FW: CTGTTCAGGCATCCGAAGGT; Inpp5d RV: AGTGTCCTCCTCAGCCTCAT). Quantification of gene expression was based on the ΔCt method, normalizing each gene of interest on the mean of the three housekeeping genes.

Bulk RNAseq analysis of mouse microglia
Cell Preparation

Hippocampal microglia were isolated from control (4 male) and cKO (3 male) mice at P15-P16. Both hippocampi of the brain were dissected on ice and quickly homogenized in 1 mL cold medium A (HBSS, 0.586% Glucose, 15mM HEPES, 2% BSA. Sigma-Aldrich, #G8270. Roth, # 9157.1). Ten strokes with a loose pestle, followed by ten strokes with a tight pestle, were done in a 2mL Dounce homogenizer. 70μm cell strainer (pluriSelect, #43-10070-50) was pre-wet with 100μL medium A and the homogenized solution was let pass through it, collecting the flowthrough in 5mL Eppendorf tube placed on ice. Percoll gradient was prepared in 15 mL plastic FACS tubes (from first to last solution: 2.4 mL cold HBSS, 4 mL cold Percoll 22.5% in HBSS 1X + 2% BSA. Sigma-Aldrich, #GE17-5445-02). 3mL of 90% Percoll in 10x HBSS with phenol red (Thermo Fisher Scientific, #14170138) + 2 BSA% were mixed with the homogenized solution and the total 4mL were placed at the bottom of the Percoll gradient. Tubes were centrifuged at 800g x 25 minutes at 4°C (acceleration 4 and no brakes). At the end of the centrifugation, myelin disk was removed, and the ring of enriched microglial cells was collected in a new 15 mL tubes and washed with 13 mL of 2% BSA in PBS 1X (Thermo Fisher Scientific, #10010-056). Samples were further centrifuged at 500g x 10 minutes at 4°C and the pellet was resuspended in 200μL of MACS buffer. Microglial cells were fluorescently sorted by means of FACS, gating for YFP⁺/DAPI⁻/ RedDot™1 Far-Red Nuclear Stain⁺ (Anawa, #40060), directly in IB lysis buffer from SPLIT RNA Extraction Kit (Lexogen, #K00848). RNA extraction was performed following the manufacturer's instructions. RNA DNBSEQ Eukaryotic Transcriptome was later sequenced by BGI genomics, using as reference genome mm39 version (Bowtie2 was utilized to align the clean reads to the reference genes).

RNA-seq analysis of mouse microglia

RNA-Seq reads were mapped to the mouse genome (GRCm38, version M12 (Ensembl 87)) with STAR (Dobin et al., version-2.7.3a[89]) using the following parameters –outSAMunmapped Within –outFilterType BySJout –outFilterMultimapNmax 20 –alignSJoverhangMin 8 –alignSJDBoverhangMin 1 –outFilterMismatchNmax 999 –outFilterMismatchNoverLmax 0.04 –alignIntronMin 20 –alignIntronMax 1000000 –alignMatesGapMax 1000000. Reads were assigned to genes using FeatureCounts (Liao et al., version-v2.0.0[90]) with the following parameters: -T 2 -t exon -g gene_id -s 2. For the differential expression analyses we used DESeq2 (Love et al., version-1.32.0[91]) with default parameters. We filtered genes that had less 5 counts in at least 3 samples. The gene set enrichment analysis was carried out using CERNO algorithm from R tmod package (Zyla et al., Bioinformatics, version-0.50.07[27]). The raw data for the bulk RNA-seq experiments have been deposited to the GEO repository are accessible through GEO Series accession number GSE268277.

Single nuclei RNA sequencing of mouse hippocampi
Nuclear isolation, library preparation, and sequencing

Nuclei were isolated from fresh frozen dissected hippocampi from one hemisphere from P15 pups (N=4 per genotype, mix sexes) as previously described.[31,99] In brief, hippocampi were lysed in a sucrose lysis buffer (10 mM Tris–HCL (pH 8.0); 320 mM sucrose; 5 mM CaCl2; 3 μM Mg(Ac)2; 0.1 mM EDTA; 1 mM dithiothreitol (DTT) and 0.1% Triton X-100). The lysates were filtered through a 70 μm cell strainer. Nuclei were purified by ultracentrifugation (107,000× g for 1.5 h at 4 °C) through a dense sucrose buffer (10 mM Tris–HCL (pH 8.0); 1.8 M sucrose; 3 μM Mg(Ac)2; 0.1 mM EDTA and 1 mM DTT). The supernatants were removed, and pellets were re-suspended in 2% BSA/PBS containing RNase inhibitor (0.35 U/μL) (Thermo Fisher Scientific). Samples were kept on ice throughout

the isolation and staining procedure. The nuclei were incubated with fluorescently conjugated antibodies directed against the neuronal marker NeuN (NeuN clone A60, AF488 mouse mAB, Merck MAB377X) and the transcription factor Olig2 for the oligodendrocyte lineage (Anti-Olig2 AF647 rabbit pAb, Novus Biologicals, NBP2-41269). After washing, the DNA dye DAPI was added, and nuclei were sorted on a MoFlo Astrios. For each sample, we separately collected DAPI+/NeuN-/Olig2- nuclei (double negatives), DAPI+/NeuN+/Olig2- nuclei (neurons), and DAPI+/NeuN-/Olig2+ nuclei (oligodendrocyte-lineage cells).

Approximately 42000 nuclei per sample were loaded onto the Chromium single cell chips (10x Genomics), with each sample consisting of all double negative nuclei, supplemented with an equal amount of neuronal and oligodendrocyte-lineage nuclei up to 42000. This strategy has previously been used to enrich for less abundant CNS cell types.[31] Single-nucleus cDNA libraries were con-structed and dual-indexed using the Chromium Single Cell 3′ Reagents Kit v3 and corresponding user guide (10× Genomics). All samples were pooled in equimolar ratios and sequenced on a NextSeq 2000 platform (Illumina) at the sequencing facility of the UMCG. Libraries were sequenced to a saturation of >30%.

Single nuclei RNASeq data analysis
Integration and pre-processing
After pre-processing with CellRanger7, nuclei were processed per sample to adjust for ambient RNA using SoupX,[92] and then to re-move predicted doublets with Scrublet.[93] Data were then loaded into Seurat v4.3,[94] retaining only features expressed in at least 3 nuclei, and filtering out nuclei that did not have 200 features, or had more than 5% mitochondrial gene expression. Samples were then merged into one object and normalized, after which the top 2000 variable features were identified. To aid in differentiating microglia, the top 75 genes detected in the bulk RNASeq dataset (based on logCPM values) were added to the variable features. Counts were then scaled while regressing for total RNA count, percent mitochondrial gene expression, and percent ribosomal gene expression. The first 50 principal components were calculated, which were loaded into Harmony[95] for integration. Post-integration, neighbors and clusters were calculated from the Harmony reduction, which were visualized using UMAPs. This resulted in 47313 nuclei, which were predominantly neurons (35407 nuclei), as evidenced by Snap25 expression. Neurons could then be split as excitatory (Slc17a7 expressing, 31961 nuclei) or inhibitory (Gad1, Gad2 expressing, 3446 nuclei). Excitatory neurons could be split as originating from the hippocampus (19326) or entorhinal cortex (12635) based on Gria1 and Tshz2 expression, respectively. More detailed re-clustering and annotations were then separately performed on the non-neuronal, excitatory neuron, and inhibitory neuron subsets. Data processing of these subsets was similar to that done for the total object, except that the top 4000 variable genes were used for integration. During these clustering steps, low quality cells (e.g., low counts, high doublet scores, expression of markers of multiple cell types) were removed. Marker genes from each cluster (calculated using the Seurat function FindAllMarkers with default parameters) are listed in Table S2.

Non-neuronal nuclei (Snap25-)
Clusters of expected non-neuronal hippocampal cell types were annotated based on previously described markers, including astrocytes (Slc1a2/Wdr17 expressing, 3846 nuclei), oligodendrocyte lineage cells (Pdgfra/Lhfpl3 expressing oligodendrocyte precursors, 1004 nuclei; Mbp enriched oligodendrocytes, 527 nuclei; Bcas1 enriched oligodendrocytes, 467 nuclei), Cajal-Retzius cells (Reln/Ndnf expressing, 531 nuclei), microglia (Csf1r/Dock2 expressing, 388 nuclei), endothelial cells (Flt1/Mecom expressing, 260), mural cells (Cspg4/Pdgfrb expressing, 288 nuclei), and ependymal cells (Cfap299/Ttr expressing, 577 nuclei). Several clusters of vascular leptomeningeal cells, as previously described,[100,101] were also found, including fibroblast-like cells (Lama1/Ptgds expressing, 2574 nuclei) and two clusters of arachnoid barrer cells (one expressing Slc47a1/Slc4a10, 1324 nuclei, another expressing Dpp4/Fn1, 120 nuclei).

Interneurons (Snap25+/Gad1+/Gad2+)
we used the molecular markers Lhx6 and Adarb28 to identify interneurons from the medial and caudal ganglionic eminences (MGE/CGE), respectively. We also found a cluster of Lamp5 expressing interneurons that expressed both the MGE marker Lhx6 and CGE marker Adarb2, as has been described in the cortical interneurons of mice, macaques, and humans.[102,103] MGE interneurons could be split into two populations, based on Sst and Pvalb expression, while CGE interneurons formed two clusters, which could be split based on Cck and Vip expression. Two interneuron clusters also resembled subtypes of cortical interneurons reported in literature based on location: neurogliaform interneurons (based on Gad1/Reln/Ndnf expression) that are present in the CA1,[104,105] and interstitial neurons (based on Meis2 expression) thought to be present in white matter.[106,107]

Excitatory Neurons (Snap25+/Gad1-/Gad2-)
A large proportion of excitatory neurons clustered based on location in the hippocampus. This was evident when plotting the top 100 marker genes as module scores on an example Visium spatial transcriptomics publicly available on the 10x Genomics website (https://www.10xgenomics.com/datasets/adult-mouse-brain-coronal-section-fresh-frozen-1-standard), which could identify a cluster whose markers resembled cornu ammonis (CA) 1 spatial transcriptomic profiles, a CA1-subicular cluster (with overlap to CA1 nuclei but also expressing Ndst4), a CA3 cluster (enriched for Grik4), and a dentate gyrus (DG)-associated cluster (enriched for Prox1). We also found an excitatory cluster whose spatial profile corresponded to the fimbria, and a small cluster resembling mossy cells in the hilus that also expressed the mossy cell marker Calb2. Beyond hippocampal neurons, we also found excitatory neurons that corresponded to various layers in the entorhinal cortex. This included two layer 2 clusters (Reln and Wfs1 expressing, respectively), a layer 3 cluster (Igfbp5/Trps1 expressing), a layer 5 cluster (C1ql3/Ncam2 expressing) and two pairs of deep layer clusters with markers for layer 6 neurons from the medial (Col5a1/Cdh18 expressing) and lateral (Kcnab1 expressing) entorhinal cortex.

CellPress
OPEN ACCESS

Immunity
Article

For the purpose of some analyses, we have aggregated neuronal sub-clusters into inhibitory, excitatory hippocampal and excitatory entorhinal clusters.

Downstream analyses

To test differential gene expression of the annotated cell types between WT and KO, we first made a pre-selection of genes per cluster that were (1) expressed in at least 5% of nuclei in one of the two groups, and (2) had an absolute log2FC of at least 0.15 between the two groups. We then used the zlm from the R package MAST (1.24.1) to identify differentially expressed genes after correcting for cellular detection rate per gene and the donor-related structure in the data. Genes were considered differentially expressed based on a false discovery rate adjusted p-value threshold of 0.05. A summarized list of number of DEGs in each cell type is reported in Table S2. Synapse-specific GO enrichment was analyzed using SynGO.[41] Differences in cell-cell communication between WT and KO mice were bioinformatically predicted using CellChat (1.6.1).[42]

The raw data for the snRNAseq experiments have been deposited to the GEO repository and are accessible through GEO Series accession number GSE264452.

Codes for snRNAseq data analysis are accessible to: https://github.com/jmkotah/SHIP1_snRNASeq_analysis

Proteomics

Proteomic analysis was performed by Protein analysis facility (PAF) at the University of Lausanne. Briefly, hippocampi from control and SHIP1 cKO littermates (3 control males and 3 control females vs 3 cKO males and 3 cKO females) were homogenized and protein concentration was measured by means of tryptophan quantification. Proteomic analysis was carried out with nanoLC-MS/MS long run. After contaminants removal, 7477 Proteins were identified in all samples. Analysis was performed using CERNO,[27] a second generation gene set enrichment algorithm, which does not rely on the arbitrary cutoffs, but on the sorted (by the p-value) list of genes. The mass spectrometry proteomics data have been deposited to the ProteomeXchange Consortium via the PRIDE partner repository with the dataset identifier PXD052118.

Intracerebroventricular injection of AAV

P0-P1 control and SHIP1 cKO pups were anesthetized with isoflurane inhalation (induction 0.8-1.5 L/min, 4-5%; maintenance 0.8-1.5 L/min, 3%) and placed over a heating pad to maintain the body temperature. Pinch reflexes were gently monitored and the needle of a 5μL Hamilton syringe was perpendicularly inserted at 2/5 of a hypothetical line connecting the lambda point to the closest eye. 2μL (2.60E^{12} vg/mL) of either AAV-mScarlet or AAV-CD55-p2A-mScarlet (generated by BrainVTA) were injected manually per hemisphere. The litters were injected with 40μL of tamoxifen (dissolved in 10% EtOH and 90% Corn Oil, at 2 mg/mL. Sigma-Aldrich, #T5648) at P3 and P4. Toe clipping of pups was performed between P6 and P12 and brains were collected at P15.

Electrophysiological recordings of CA1 pyramidal neurons

Male and female animals (P15 to P18 pups) were deeply anesthetized with isoflurane before decapitation, and coronal sections (250-μm thick) containing hippocampus were sliced using a vibratome (VT1000S, Leica, Wetzlar, Germany) in oxygenated 4°C slushy cutting solution containing (in mM): 110 choline chloride, 2.5 KCl, 1.25 NaH2PO4, 7 MgCl2, 0.5 CaCl2, 11.6 ascorbic acid, and 3.1 sodium pyruvate, 25 NaHCO3 and 25 glucose (295 to 305 mOsm). Right after slicing, sections were transferred in the same solution kept at 32°C for 5 min then in oxygenated ACSF recording solution for at least 1 h before starting recordings. Experiments were performed using a BX51WI upright microscope (Olympus, Tokyo, Japan) mounted on a motorized stage and coupled to micromanipulators (Sutter Instruments, Novato, USA). After resting, slices were transferred in a submerged-type recording chamber under the microscope (JG-23W/HP, Warner Instruments, Hamden, USA) and continuously superfused at a flow rate of 2 ml/min with oxygenated ACSF recording solution maintained at 32-34°C and containing (in mM): 124 NaCl, 2.5 KCl, 1 NaH2PO4, 1.3 MgCl2, 2.5 CaCl2, 26.2 NaHCO3, and 11 glucose (295 to 305 mOsm). Borosilicate glass pipettes (Harvard Apparatus, Holliston, USA) with tip resistances ranging from 4 to 6 MΩ were shaped with a horizontal micropipette puller (DMZ Universal electrode puller, Zeitz Instruments, Munich, Germany) and used to obtain whole-cell recordings from visually identified CA1 pyramidal neurons of hippocampus. The intrapipette solution contained (in mM): 120 cesium methansulfonate, 10 HEPES, 10 CsCl, 10 EGTA, 5 Na-phosphocreatinine, 2.5 MgATP, and 0.25 NaGTP (pH 7.2–7.3; 280 ± 5 mOsm). Whole-cell recordings were performed using a MultiClamp 700B amplifier associated with a 1440A Digidata digitizer (Molecular Devices, San Jose, USA). Neurons were voltage clamped at −60 mV in the presence of picrotoxin (PTX, 100 μM) to block GABA A receptor-mediated inhibitory postsynaptic currents and to isolate spontaneous AMPAR-mediated excitatory postsynaptic currents (sEPSC) and tetrodotoxin (TTX, 1μM) was applied in addition to PTX to isolate miniature AMPAR-mediated excitatory postsynaptic currents (mEPSC). Neurons with an access resistance exceeding 25 MΩ or changed by more than 20% during the recording were excluded. Bridge balance and pipette capacitance were adjusted before recording. EPSC were filtered at 2 kHz, digitized at 10 kHz, and collected online using pClamp 10 (Molecular Devices, San Jose, USA). Quantitative analysis of sEPSC and mEPSC were performed using the Mini Analysis software (Synaptosoft, Decatur, USA).

Genomic integrity of human iPSC lines

The WTC-11 iPSC line was tested for genomic integrity at passage 36 using SNP-array technology (Global Diversity Array v1.0 BeadChip, Illumina). No detection of CNV larger than 1.5Mb or AOH larger than 3Mb were detected on somatic chromosomes. The typical WTC-11 deletion of 2.9Mb on Yp11.2 was detected. This deletion is known to be present in the donor, from whom the

Immunity
Article

CellPress
OPEN ACCESS

cell line was derived [PMID: 23862100]. The same assay was performed on the *INPP5D* knockout iPSC clones and showed no significant differences in genomic integrity as compared to parental WTC-11 PSC.

hiPSC genomic stability assay
Analysis of genomic stability of iPSCs
Virtual Karyotype analysis was performed by Infinium Global Diversity Array-8 v1.0 (Illumina). Data analysis was conducted with VIA software (Bionano). CNVs or AOH encompassing regions smaller than 1.5 Mb were not considered.
RNA analysis
Transciptome analysis of iMG microglia was performed using Kallisto transcriptome indexing using GRC38 and inhouse pipeline. Raw count files from our study of control and SHIP1 KO iMG, dataset from Abud et al. (GSE89189) and Drager et al. (GSE178317) were downloaded and merged to plot principal component for Microglia, HPC, iPSC, Monocytes, Dendritic cells, Fetal microglia, Adult microglia,[60] iTF microglia and BrownJohn microglia[59] with our control and SHIP1 iMG microglia. The raw data for the bulk RNA-seq experiments on iMG have been deposited to the GEO repository are accessible through GEO Series accession number: *to be confirmed*.
Western Blot for iMG characterization
Lysates were prepared with Lysis buffer M-PER™ (Thermo Fisher Scientific, #78501) with 1x Protease and Phosphatase inhibitor (Thermo Fisher Scientific, #PI78441). 15 μg of lysate were loaded in a 4-12% Bis Tris Plus Gel for reducing SDS page (Invitrogen #NW04125BOX, NP0007, B0009) with MES (Invitrogen, #B0002). After blocking in 5% milk for 1h, the membrane was incubated with primary antibodies at the following dilutions in 5% milk: SHIP1 1:1000 (Santa Cruz, #P1C1), GAPDH 1:20000 (Abcam, #ab181602) and IBA1 1:1000 (Merck Millipore, #MAbN92). After washes in TBST, the membrane was incubated with secondary antibodies (Vector laboratories PI-1000, PI-2000) in 5% milk at 1:10000. Blots were developed with WesternBright ECL (Advasta, #K-12045-D20) for GAPDH and IBA1, while SHIP1 was detected using Supersignal West PICO (Thermo Fisher Scientific, #34577). Results are representative of two differentiations for both clones.
Immunofluorescence staining
Microglia were seeded on Matrigel coated 96 well plate at 1*10^5/mL. After 24h cells were fixed with 4% PFA for 20 minutes and permeabilized with 0.1% Triton-X100 in PBS for 30 minutes. After 3 washes, the samples were blocked with 1% BSA in PBS for 1h at RT and incubated with IBA1 primary antibody 1:500 (Merck Millipore, #MAbN92) for 1h at 37°C. Cells were washed and incubated with secondary antibody 1: 1000 (Thermo Fisher Scientific, #A-21141) and incubated 1h at 37°C. Samples were washed, incubated with 300nM DAPI (Thermo Fisher Scientific, #D1306) in PBS and acquired using Keyence imager BX-800 at 20x magnification.
Synaptosome preparation and labeling
IPSC-derived neurons were differentiated from neural precursor cells (NPCs) of WTC11 donor line using established protocols.[108] Synaptosomes were prepared from 6 weeks old neurons with SynPer buffer (Thermo Fisher Scientific, #87793) using manufacturer recommendation and as previously described.[58] After quantification of Synaptosome preparation in PBS with BCA (Thermo Fisher Scientific, #23225), labeling with pHrodo Red (Thermo Fisher Scientific, #P36600) was performed using manufacturer recommendation using 52ng of reactive Dye for 100μg of protein. Final synaptosome preparation was stored in PBS containing 5% DMSO in -80°C.
Phagocytosis assay
Microglia were gently detached with Accutase and plated at 1*10^5/mL on a Matrigel coated 96 well plate with 100 μL of 5F media per well. After 24h from seeding, cells were incubated with 1μg of pHRodo-labeled human synaptosomes per well. The acquisition was performed with live imaging using the Incucyte® S3 Live-Cell Analysis System at 37°C and 5% CO2. Automatic masking and quantification were performed with the Sartorius Live-Cell Imaging and Analysis Software with Adherent Cell-by-Cell analysis for Red Integrated Intensity on the masked area (RCUxmm^2). For Bafilomycin and Cytochalasin control experiments: microglia were incubated with 100nM Bafilomycin, 1 μM CytochalasinD or DMSO control in presence of pHrodo-labeled synaptosomes. After 17h cells were fixed and imaged with 20x confocal microscopy Zeiss LSM inverted microscope.

EVs isolation from BV2
EVs were isolated by ultracentrifugation using the same protocol as in Leggio et al.[109] Briefly, the day before EVs isolation, control and SHIP1 KO BV2 cells were washed with PBS 1X and cultured in medium supplemented with 10% FBS depleted of exosomes (GibcoTM, #A2720801), for 24 h. Then, cell culture media were collected and centrifuged at 1000 x g at 4°C for 15 minutes to eliminate cell debris and residual cells. The resulting supernatants were transferred in ultra-cone polyclear centrifuge tubes (Seton, #7067) and subjected to ultracentrifugation using the swing-out rotor SureSpin 630 (k-factor: 216, RPM: 23200) in a Sorvall WX100 (Thermo Fisher Scientific). The first ultracentrifugation was performed at 100,000 g at 4°C for 75 minutes. The supernatants were discarded, and the pellets were washed with cold PBS 1X and ultracentrifuged again at the same speed for 40 minutes in thick wall polycarbonate tubes (Seton, #2002), using the fixed-angle rotor T-8100 (k-factor: 106, RPM: 41000). The resulting pellets were resuspended in PBS 1X for NTA or in RIPA buffer for WB characterization.
Nanoparticle Tracking Analysis (NTA)
EV concentrations and size were determined using the Nanosight NS300 analyzer (Malvern, United Kingdom). EV preparations were diluted to achieve a particle concentration of 30-80 particles per frame, prior to injection into the sample chamber at a constant flow rate (100 arbitrary units). Camera level was set to 15 and three 60 seconds videos were then acquired and analyzed to obtain the

particle concentration and size data. For all samples, detection threshold was set as 5 and all other setting were set to "automatic".

Western blot for EVs

Cells and EVs extracts were processed as in Leggio et al.[109] Briefly, cells and EVs were lysed in RIPA buffer (10 mM Tris HCl pH 7.2 (Fisher Scientific, #BP152); 150 mM NaCl (Sigma Aldrich, #S7653); 1% Sodium deoxycholate (Sigma Aldrich, #30970); 0,1% (for cells) or 3% (for EVs) SDS (Sigma Aldrich, #71736); 1% Triton X-100 (Sigma Aldrich, #T8787); 1 mM EDTA pH 8 (VWR chemicals, #E177-100ML); 1X Complete Protease inhibitor cocktail (Roche, #04693116001); 1 mM Phenylmethanesulfonyl fluoride solution (PMSF, Sigma Aldrich, #93482); 1X Halt Phosphatase inhibitor cocktail (Thermo Fisher Scientific, #78420), and protein concentration was measured with DC Protein Assay (Biorad, #500-0116), using BSA (Pierce, #23210) as standard. The same amount of cell or EV lysates were loaded into 4-12% Bis-Tris plus gels (Invitrogen, #NW04125BOX) in non-reducing conditions. Proteins were transferred onto PVDF membrane. All primary and secondary antibodies are: CD63 1:5000, MBL, #D263-3; CD9 1:5000, BD Pharmigen, #553758; Calnexin 1:10000, Abcam, #ab22595; β-Actin 1:10000, Sigma-Aldrich, #A1978. HRP-conjugated anti-rat secondary antibody 1:10000, Invitrogen, #31470; HRP-conjugated anti-rabbit secondary antibody 1:10000, Invitrogen, #31460; HRP-conjugated anti-mouse secondary antibody 1:10000, Dako, #P044.

Behavioral testing

All behavioral experiments were performed on male and female littermates, during the light phase of the light/dark cycle. Animals were handled for one week before starting behavioral tests.

Open Field Test (OF)

The animals were placed in a plexiglass box (45cmx45cmx40cm) and they were video recorded for 20 minutes (2 trials, 10 minutes each, 30 minutes between trials). The light intensity in the arena was set at 10-15 lux. Analysis of the first 10 minutes of exploration was performed using Ethovision software, assessing distance travelled and time spent in the center. This test was also used as habituation for the subsequent Novel Object Recognition Test.

Novel object recognition (NORT)

It was performed 24 hours after the OF, maintaining the same light intensity. On the training day, in the same OF arena, mice were exposed to two identical objects (placed in two opposite corners), defined as familiar objects. The animals were free to explore those objects for 10 minutes. 24 hours later, one of the two items was replaced with a novel one, and mice were let explore the objects for 10 minutes (Test Phase). All the exploration were video recorded, and the time spent sniffing the objects was manually counted offline.

Y-Maze

Mice were placed in the center of a three-arm plexiglass maze (arm length 35cm, arm width 6cm, height 16cm) and they were let free to explore the three arms of the maze for 5 minutes. The light intensity was set at 10-15 lux. The performance was video recorded and analyzed offline. The correct number of alternations in the arms entry was evaluated.

Rotarod

Mice were placed on a rotating rod for 5 minutes, in three consecutive trials (intertrial time: 5 minutes). The rotation increased gradually (4 RPM, with acceleration to 40 RPM, over the course of 300 seconds), and the latency to fall was analyzed and shown as a sum of the three trials. *Barnes Maze*: The light intensity was set at 40-50 lux. Mice underwent 4 consecutive days of training. On each training day, the animals received 4 trials. Each trial consisted of 3 minutes, in which the mice explored a round platform (100cm diameter) with 20 holes (5cm diameter each, 4cm distant from the edge) only one of which led to the escape box. Each trial ended when the animal found the escape box, or when 3 minutes elapsed (if so, mice were helped to find the escape box). The latency to first reach the escape box was assessed by using Ethovision software. After 4 days of training, the animals underwent the test phase, which lasted 90 seconds. In this phase, the escape box was removed, and the time spent by the mouse in the target quadrant (previously containing the escape) was measured by Ethovision software. The performance of the mice was videotracked.

QUANTIFICATION AND STATISTICAL ANALYSIS

Data representation, statistical testing and outliers' identification were performed using GraphPad Prism (10.2.2). Results are represented as mean ± standard error of the mean (SEM). Two-tailed unpaired t-test, multiple t-test, one- or two-way analysis of variance (ANOVA) where used as appropriate. Detailed statistics used, p-values and number of biological replicates are reported in each figure legend.